UNIVERSITÀ DEGLI STUDI DI PADOVA

Dipartimento di Fisica e Astronomia "Galileo Galilei"

Corso di Laurea Magistrale in Astronomia

Tesi Magistrale

Investigating the effect of redshift and host galaxy on the multiple-population phenomenon

Relatore

Prof. Antonino P. Milone

Correlatori

Dott. Edoardo Lagioia

Dott.ssa Anna F. Marino

Laureando

Emanuele Dondoglio

Anno Accademico 2019/2020

Contents

1 Introduction **3**
- 1.1 Multiple Populations in Globular Clusters . . . 3
  - 1.1.1 Observational Properties of Multiple Populations in Globular Clusters . . . 7
- 1.2 Formation Scenarios of Multiple Populations . . . 8
  - 1.2.1 Supermassive Stars (SMS) . . . 8
  - 1.2.2 Fast Rotating Massive Stars (FRMS) . . . 9
  - 1.2.3 Massive Interacting Binaries (MIB) . . . 9
  - 1.2.4 AGB Stars . . . 10
- 1.3 Magellanic Cloud Clusters . . . 10
- 1.4 Outline and purpose of the Thesis . . . 12

2 Data and Data Analysis **13**
- 2.1 Instrumentation . . . 13
- 2.2 Dataset . . . 14
- 2.3 Effective Point Spread Function Photometry . . . 15
  - 2.3.1 The effective Point Spread Function . . . 15
  - 2.3.2 Deriving the effective Point Spread Function Model for NGC 416 . . . 16
- 2.4 Building the Catalog . . . 18
  - 2.4.1 Bright Star Analysis . . . 18
  - 2.4.2 Faint Stars Analysis . . . 21
- 2.5 Calibration . . . 22

3 Results **25**
- 3.1 Differential Reddening Correction . . . 25
- 3.2 Population ratio from the red HB . . . 28
- 3.3 Multiple populations along the red HB . . . 30
  - 3.3.1 A new tool to disentangle multiple populations along the red HB . . . 30
  - 3.3.2 Extragalactic Globular Clusters . . . 34
- 3.4 NGC 6362 . . . 37
- 3.5 NGC 6388 and NGC 6441 . . . 37

4 Discussion and conclusion **43**
- 4.1 Correlations with Cluster Parameters . . . 43
- 4.2 Comparison with the literature . . . 44
- 4.3 Summary and Conclusions . . . 50

Chapter 1

Introduction

In this Chapter, I provide the modern view of globular clusters (GCs), which are now considered complex stellar systems composed of multiple stellar populations (MPs). In Section 1.1 I illustrate the main photometric evidence of MPs, telling a brief history of the change in perspective about the nature of these objects, and explaining the main tools used to detect MPs. Section 1.2 shows the main observational properties of MPs and some theoretical scenarios that could explain their formation in GCs. Section 1.3 explains the differences between the Galactic and the Magellanic Clouds (MCs) GCs. Section 1.4 summarizes the outline and the aim of the thesis.

1.1 Multiple Populations in Globular Clusters

Since a few years ago, GCs were considered as prototypes of Single Stellar Population (SSP), therefore composed by stars that are coeval, chemically homogeneous and distributed according to a well defined Initial Mass Function (IMF). In fact, from high precision photometry, the typical sequences in the Colour-Magnitude Diagram (CMD) were quite narrow, validating this hypothesis.

New techniques of photometric data reduction were subsequently introduced by Anderson & King (2000). These were based on the so called effective Point Spread Function (PSF), which allows a more accurate estimate of stars position and magnitude. This approach is effective in crowded star fields, usually observed by the Hubble Space Telescope (HST). Using this method, and considering diagrams sensitive to chemical differences between stars, it has been possible to understand that GCs actually host MPs.

But which are these diagrams? Many photometric tools have been developed in the recent years. Combining optical and near infrared (NIR) with ultraviolet (UV) photometry, makes possible to build CMDs with a wide colour baseline. This has revealed to be very useful, because MPs are very sensitive to differences in Carbon (C), Nitrogen (N) and Oxigen (O), which brings to variations in magnitude in UV filters, due to the fact that molecular bands of OH, NH, CH, and CN affect this region of the spectrum (Piotto et al. 2015). Furthermore, a wide colour baseline allows to detect smaller effective Temperature (T_{eff}) variations, therefore Helium (He) variations, which acts on the T_{eff} of stars. Stars that are He-enhanced are hotter (therefore bluer) than the ones with

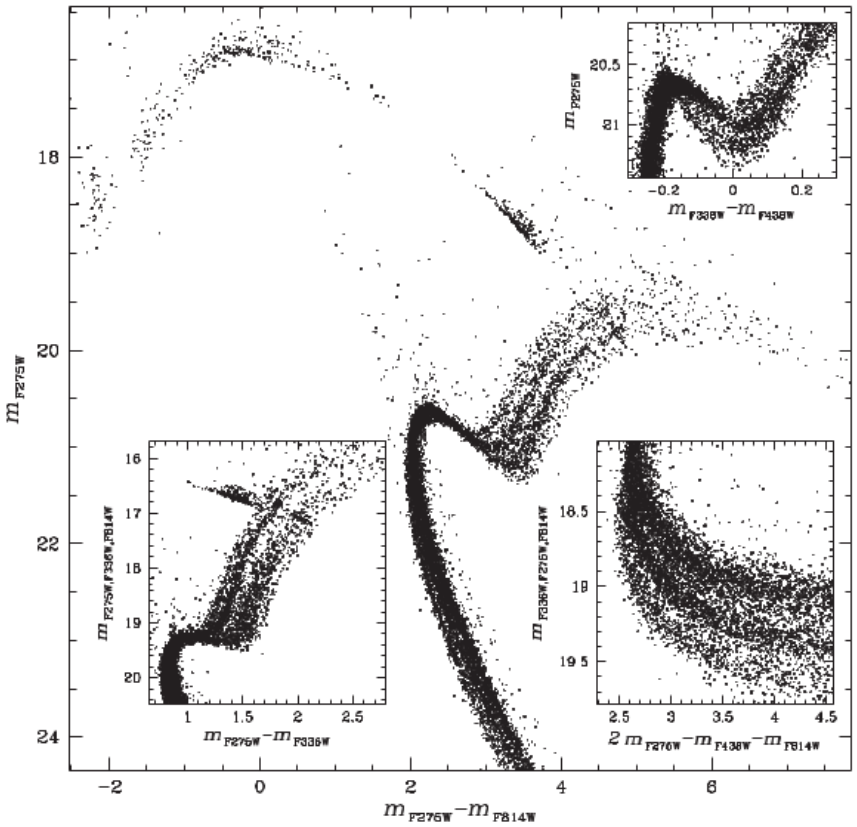

Figure 1.1: Example of CMD sensible to He variations (Milone et al. 2015). It shows, for NGC 2808, the presence of separated star sequences. In the other three small panels, filter combinations that can highlight particularly well the separation in MS, SGB and RGB are shown.

primordial He abundance ($Y \sim 0.25$) and similar magnitude (D'Antona et al. 2002). An example of the effectiveness of this approach is given in Milone et al. (2015), where MPs along the Main Sequence (MS) and Red Giant Branch (RGB) for NGC 2808 appear well separated, using diagrams given by the combination of UV, optical and NIR filters, as it is shown in Figure 1.1.

But not only the classical CMDs are useful to separate MPs. Using combinations of magnitudes in $F275W$, $F336W$ and $F438W$ filters of UVIS/HST, it is possible to build diagrams that can efficiently separate populations with different abundances in light elements. The following diagrams are presented considering these three filters. However, they can be substituted with other filters that cover a similar spectral range, so that are sensitive to the same abundances, like $F225W$, $F343N$ and $F410M$, obtaining the same separation. One important tool in separating MPs is the index $C_{F275W,F336W,F438W} = (m_{F275W} - m_{F336W}) - (m_{F336W} - m_{F438W})$ (Milone et al. 2013), which has the advantage of separating multiple sequences with different N abundances along the whole CMD, for example in diagrams like m_{F275W} vs $C_{F275W,F336W,F438W}$ or m_{F336W} vs $C_{F275W,F336W,F438W}$, as shown in panel (c) of Figure 1.2. In

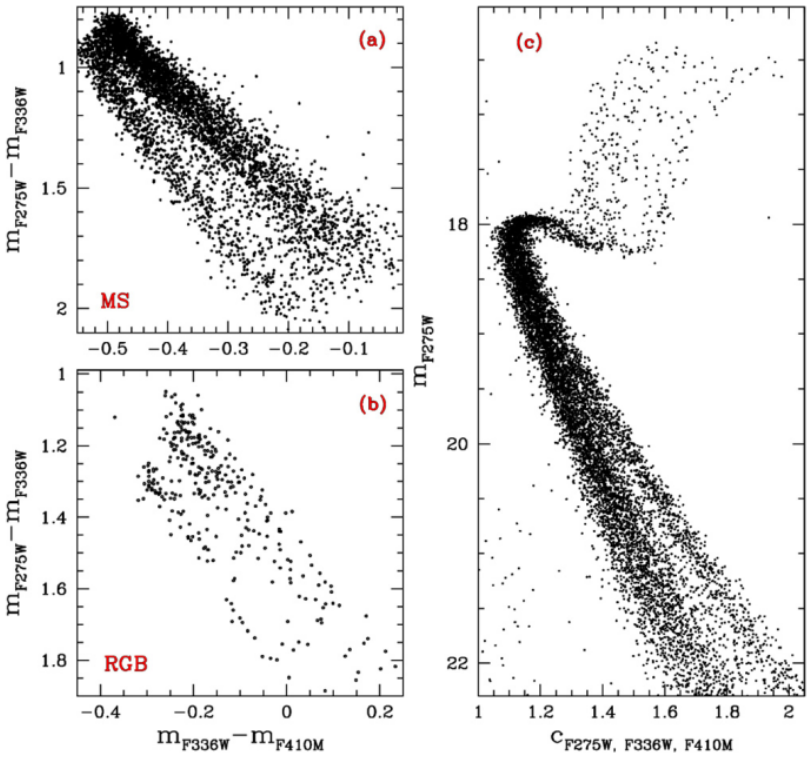

Figure 1.2: Example of diagrams useful to separate MPs for NGC 6752 (Milone et al. 2013). In panel (c) is represented the m_{F275W} vs $C_{F275W,F336W,F410M}$, in panel (a) and (b) are represented the two-colour diagrams $m_{F336W} - m_{F410M}$ vs $m_{F275W} - m_{F336W}$ for MS and RGB respectively.

Milone et al. (2015), it was also introduced the so-called Chromosome Map (ChM), a diagram that maximizes the information about the differences in chemical composition for MS, RGB and Asymptotic Giant Brach (AGB) stars. As explained in the paper, the ChM was built starting from diagrams such as m_{F814W} vs $m_{F275W} - m_{F814W}$ and m_{F814W} vs $C_{F275W,F336W,F438W}$, measuring the variation of the two quantities at the abscissa for each star with respect to a certain fiducial line, obtained as explained in Piotto et al. (2007). The ChM map is then the diagram of these variation, $\Delta Y(F275W, F336W, F438W)$ vs $\Delta X(F275W, F814W)$. If stars had all the same chemical composition, typical of galaxy field stars, they would form a small blob centered in $(0, 0)$ on the ChM. Instead the observed distribution is wider. This of course shows the presence of stars with different chemical composition, combining information from the CMD m_{F814W} vs $m_{F275W} - m_{F814W}$, sensitive to He variations, with the ones from m_{F814W} vs $C_{F275W,F336W,F438W}$, sensitive to N variations. An example can be seen in Figure 1.3.

The last tool here reviewed, which is largely used in this thesis, is the two-colour diagram $m_{F336W} - m_{F438W}$ vs $m_{F275W} - m_{F336W}$, that can be seen in panels (a) and (b) of 1.2. It allows to separate stars with different chemical abundances in He, C, N and O, as showed in Milone et al. (2012d) for 47 Tuc,

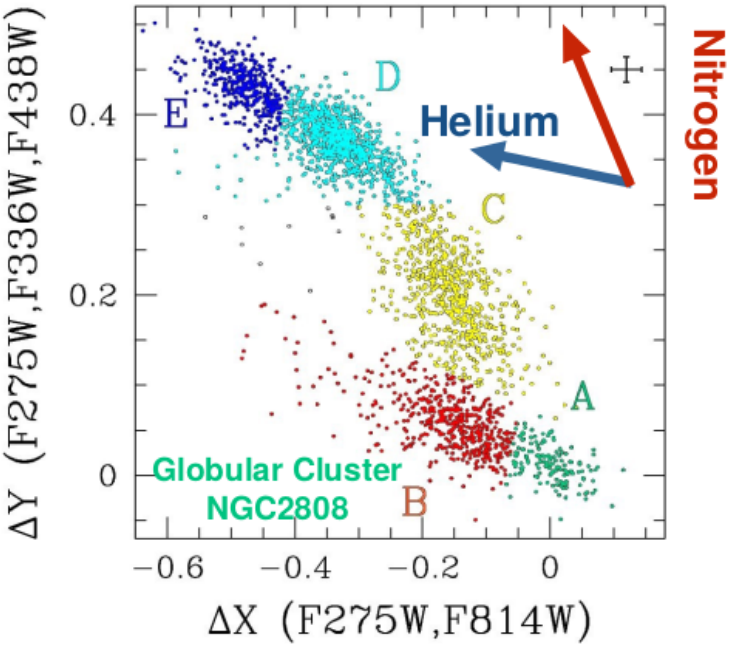

Figure 1.3: Example of a ChM for NGC 2808 Milone et al. (2015). Each group of stars is identified with different colours and letters. Population A represents the 1G stars. The other four groups are all 2G stars with different abundances. The two arrows shows in what direction stars are more enriched of He and N.

distinguishing two families of stars along MS, SubGiant Branch (SGB), RGB and Horizontal Branch (HB).

These observational evidences have brought to the definition of two families of stars: the first generation (1G) and the second generation (2G). The 1G stars have a chemical composition similar to the one of the galactic field stars (like Milky Way halo stars), as expected in a SSP model. In fact these stars lie near the "origin" of the ChM. On the other hand, the 2G stars are the ones with unique abundances in light elements like He, C, N, O and Na, and they were only found inside GCs. It is interesting then to investigate how these abundances vary between the two groups. As observed for example in Marino et al. (2008), Cohen & Melendez (2005) and Carretta et al. (2009), Na and O are anticorrelated from each other: the 2G are enriched in Na and are depleted in O with respect to the 1G stars. Furthermore, the 2G stars are enriched in He. Measuring the He abundances via spectroscopy is very challenging and possible only for stars with surface temperatures between $\sim 8000\ K$ and $\sim 11500\ K$. In fact, cooler stars do not have lines that are strong enough to be detected. On the other hand, hotter stars experience He settling, that results in abundances in the stellar atmosphere that are not representative of the initial He content (Behr 2003). The use of appropriate photometric diagrams, sensible to the He variations, has made possible to estimate differences in He abundances inside a cluster (Milone et al. 2015, Lagioia et al. 2018, Zennaro et al. 2019).

1.1.1 Observational Properties of Multiple Populations in Globular Clusters

Years of observations have given not only the prove about the existence of MPs in GCs, but they also brought to some constraints on the origin and formation of these MPs, that are exhaustively described in Renzini et al. (2015) and Milone (2019). Briefly, some of the observational properties of MPs in GCs are the following:

- **GC Specifity.** 2G stars seems to be present only in GCs and not in the field. In fact, 2G stars are very rare in Milky Way field: the small number is consistent with a scenario where these stars have been generated inside GCs and then lost via tidal interactions (Vesperini et al. 2010).

- **Variety.** While all GCs are considered to host MPs, there are not two equal clusters. In fact, each one has its own pattern of MPs, ranging from two in the less massive ones, like NGC 6535, to more than 10 in the most massive, like ωCen (Milone et al. 2017).

- **Discreteness.** There is not a continuous distribution of stars in the ChM. In fact, different populations form discrete sequences of stars in most of the GCs studied (Milone et al. 2017b).

- **Two classes of GC.** The use of the ChM to study MPs allows to distinguish clusters in two classes. In fact, almost $\sim$ 17% of galactic GCs studied in Milone et al. (2017) present multiple sequences of 1G and 2G stars. These are called type II clusters (or anomalous), while the remaining are called type I clusters (or normal). The existence of anomalous GCs seems caused by star-to-star difference in abundance of heavy elements in the anomalous ones, like Iron (Fe) and s-process elements (Yong et al. 2008; Marino et al. 2019).

- **Supernova avoidance.** Many GCs have 1G and 2G which share the same metallicity. Type II clusters are exceptions, as explained in the previous point. However, even considering ωCen, the Type II GC with the largest [Fe/H] variations, in order to produce the amount of Fe observed in its 2G stars it is sufficient that only 2% of the Fe ejected by core-collapse Supernovae is retained by the 2G (Renzini 2013). Therefore, 2G stars have experienced a very little contamination by Supernovae products.

- **Hot CNO and NeNa processing.** The peculiar abundances detected in 2G stars result from CNO-cycling and p-capture processes at high temperatures. Therefore, the ISM in which they have formed should be polluted by the elements resulting from these processes. A scenario that explains the phenomenon should take account of the variety of composition patterns exhibited by 2G stars of all the studied GCs.

- **Helium enrichment.** As explained at the end of Section 1.1, a photometric approach has made possible to separate populations with different He abundances, showing that 2G stars are He-enriched. This has been detected in every GC with MPs.

- **Mass budget.** Many GCs have a fraction of 2G stars compared to the total number which is predominant. This is a challenge for the formation scenarios in which the 1G are formed before the 2G. A possible explanation is that the progenitors of the present-day GCs had a larger mass, which has been lost by dynamical interaction with the Milky Way.

- **Centrally-concentrated 2G.** Some GCs, like 47 Tuc, ωCen, NGC 2808 and M 3, 2G stars are more centrally-concentrated than the 1G (Sollima et al. 2007; Bellini et al. 2009; Milone et al. 2012a; Cordero et al. 2014; Lee 2018). Other GCs, like NGC 6752, NGC 6362 and M 5, have instead a similar radial distribution of 1G and 2G stars (Nardiello et al. 2015; Dalessandro et al. 2018; Milone et al. 2019).

- **Anisotropic motions of 2G stars.** Not all GCs have the same radial velocity distribution. In fact, 2G stars of massive GCs display a more radially-anisotropic velocity distribution with respect to the 1G (Bellini et al. 2018; Richer et al. 2013). Instead, less massive GCs display an isotropic velocity distribution for each 1G and 2G (Cordoni et al. 2019). This could be due to the fact that any kinematics differences between the two at the formation, has been erased by dynamical processes.

- **Dependence on cluster mass.** The fractions of 1G stars show a strong correlation with both the present day and the initial mass (Milone et al. 2020a), displaying a larger fraction of 1G stars for less massive GCs. A consequence is that the incidence and the complexity of multiple populations both increase with cluster mass (Lagioia et al. 2019).

- **Dependence on GC orbit.** Clusters with higher perigalactic radii ($Rper > 3.5$ kpc) host a larger fraction of 1G stars than the ones with $Rper < 3.5$ kpc (Zennaro et al. 2019). This could mean that the interaction with the Milky Way during the whole cluster life has a role in 1G/2G fractions.

1.2 Formation Scenarios of Multiple Populations

Many scenarios have been proposed in order to explain the formation of MPs. Here are reviewed some of the most important ones of the latest years, following the work of Renzini et al. (2015).

1.2.1 Supermassive Stars (SMS)

This model, proposed by Denissenkov & Hartwick (2014) and Denissenkov et al. (2015), tries to explain MPs phenomenon by considering that, in the first Gyrs of the life of a GC, the most massive stars falls towards its centre because of dynamical friction and coalescence. This brings to the formation of stars with mass of $\sim 10^4$ $M_\odot$, the SMSs. The luminosity of these stars is close to the Eddington limit, causing strong and intense stellar winds. Since these stars are fully convective, they are also chemical homogeneous and as they evolve, their wind would be progressively enriched by He, products of CNO cycling and p-capture reaction. At this time of its life, a GC still contains gas that is collapsing to form stars. This collapsing gas is then polluted by the winds, forming stars

with different abundance of (in particular) He, C, N and O, which would be the 2G stars. But the SMS is also accreting nearby material which is still not collapsed into stars, providing further fuel to its burning processes. This is the so called rejuvenation, that could make the SMS life longer. Therefore, it could eject material ten times higher than its mass (Gieles et al. 2018). This would provide a solution to the mass budget problem.

However, this mechanism could not explain the observed He enrichment, which would require a SMS mass too high with respect to the one predicted by the model. The same problem is present when considering the amount of O depletion observed (Renzini et al. 2015).

1.2.2 Fast Rotating Massive Stars (FRMS)

This scenario, as explained in Krause et al. (2013), speculates about the existence of very massive stars ($\sim 25 - 150$ $M_\odot$) which are also rotating very fast ($\sim 800 - 1000$ $km\ s^{-1}$). These FRMS lose therefore material via equatorial wind, forming a disc around them, which is rich of products of H-burning. 2G stars may form from gravitational instability inside the disc.

The scenario however presents some issues. There are no reasons to not have these stars also in other part of the Milky Way, therefore 2G stars should be observed also outside GCs, in contrast to GCs specificity. An other problem is that this idea cannot explain the discreteness, because it brings to a continuous distribution of abundances. Even the Supernova avoidance requirement seems to not agree whit this scenario: Supernovae ejection should have polluted the central and very crowded region of GCs, or even erase those discs.

1.2.3 Massive Interacting Binaries (MIB)

This scenario is based on the existence of binary systems formed by massive stars ($15 - 20$ $M_\odot$). In the version proposed by de Mink et al. (2009), the rotation of the two stars around their common center of mass forces the rotation of the primary envelope, causing mixing of material inside a star. If this material reaches the H-burning shell, CNO cycling and p-capture process would be active in the the whole envelope, causing the He enhancement, the O depletion and the other abundance variations that lead to a 2G star. In fact, the processed envelope would then be spread outside the system of MIB, polluting the nearby ISM.

In the version of Bastian et al. (2013), the material ejected in MIB would be swept out by the protoplanetary discs around low-mass stars (< 2 $M_\odot$), that eventually would be accreted by the stars themselves when they passes near a MIB system.

An insurmountable problem with this scenario concerns the discreteness. Large chemical differences in the swept out/accreted material are indeed expected, but there is no mechanism that allows a quantized accretion, necessary to justify the discreteness observed in GCs. Even the Supernovae avoidance is a probem: MIB should coexist whit core collapse Supernovae (both from single stars and binary systems), therefore should be polluted not only by MIB ejecta but also by Supernovae remnants.

1.2.4 AGB Stars

Stars in the AGB phase, with masses from $3 - 4$ $M_\odot$ to 8 $M_\odot$, experience the Hot Bottom Burning (HBB) process, in which p-capture process is very efficient due to the high temperature reached in the bottom of the convective envelope (Ventura et al. 2013). In this phase, AGB stars must have a mass > 3 $M_\odot$, otherwise HBB process would not operate and AGB stars would evolve as carbon (C) stars. But no C-star has been observed, therefore the formation of 2G stars should end before > 3 $M_\odot$ stars reach the AGB phase. The mass range should then be extended up to 10 $M_\odot$ AGB stars, which ignite C in the core, producing He and CNO cycling products. The temperature at the bottom of the envelope depends on the stellar mass, but is also very sensitive to the treatment of the convective envelope, still source of uncertainties nowadays.

In the model proposed by D'Ercole et al. (2010), the GC progenitor (more massive than the actual one) has a major episode of star formation, leading to the first 1G stars. The residual non-collapsed gas is then swept out by the Supernovae ejection. After that, AGB era starts, with ejection that brings slow winds that could remains in the potential well of the GC, polluting it. Then an other (or others) starburst episode occurs, in which the 2G stars are formed starting from a mixing of pristine gas and AGB ejecta. The GC progenitor then loses a lot of 1G stars by interacting with the parent galaxy (because 2G stars are only formed in the inner part, while in the outer one there are mainly 1G stars), leaving the present-day structure.

This model does not present insurmountable problems. However, some issues can be pointed out. Considering the mass budget problem, it is solved if the progenitor is massive enough. The mass required depends on factors such as the AGB donors mass range, the star formation efficiency and the IMF of 2G. To minimize the problem D'Ercole et al. (2010) proposed a IMF truncated at 8 $M_\odot$, ensuring in this way Supernova avoidance. This would prevent core collapse events that could sweep out the remaining gas, keeping material available to subsequent formation bursts. With these consideration, the mass of the progenitor is estimated to be 5 to 10 times the present-day mass. An other difficulty that this model encounters is related to the Na-O anticorrelation. The problem is that 1G AGB donor stars lead, on the contrary, to a correlation between the two. This issue could be solved as explained in Renzini et al. (2015), considering that in AGB stars, at a temperature $< 10^8$ K, O is destroyed faster than Na. This means that in order to have 2G stars which are O depleted and Na rich, the HHB should work at this range of temperature in a suitable fraction of the AGB stars.

1.3 Magellanic Cloud Clusters

The typical galactic GCs are old, with ages between $10 - 12$ Gyr. Younger GCs have been found outside the Milky Way, such as in the Magellanic Clouds (MCs). Studying these clusters not only helps to give a clue if the 2G star formation is an event happened in the early years of the life of a GC or in a more recent epoch, but also gives information about the role of the environment on the phenomenon.

MPs have been observed in extragalactic clusters with ages similar than the

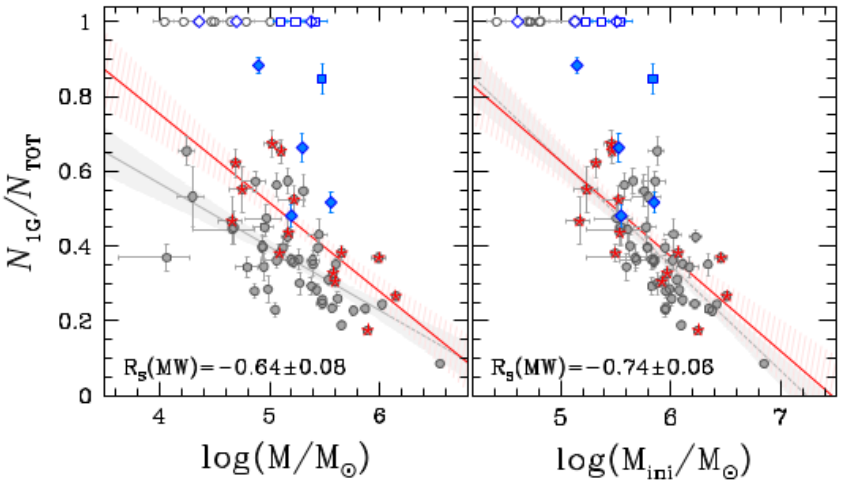

Figure 1.4: Correlation between the fraction of 1G stars and the present-day and initial masses, at left and right panels respectively (Milone et al. 2020a). The grey dots are the galactic GCs, the blue squares are the Large MC GCs, the blue diamonds are Small MC GCs. The open simbols indicates the GCs without evidence of MPs. Finally, the galactic GCs marked with the red starred symbols have $R_{PER} > 3.5$ kpc.

galactic GCs (Lagioia et al. 2019b; Martocchia et al. 2018; Niederhofer et al. 2017), suggesting that the phenomenon is not restricted to the Milky Way only. Following Cabrera-Ziri et al. (2018), the CMDs of clusters with different ages show different features:

- Young clusters, with ages < 500 Myr, present the so-called split MS, that is a MS formed by two separate sequences of stars.
- Young and intermediate age clusters, with < 2 Gyr, present the multiple MS and the extended MS Turn-Off (eMSTO), in which stars in the MS Turn-Off are distributed over a large colour interval in the CMDs.
- Intermediate age and ancient cluster, with > 2 Gyr, present multiple RGB sequences on their CMDs.

In young and intermediate age clusters, spectroscopic studies have shown that they are chemically homogeneous (Mucciarelli et al. 2014; Martocchia et al. 2017). Their splitted MS and eMSTO are attributed to different rotation (D'Antona et al. 2015; Milone et al. 2017; Bastian et al. 2018; Cordoni et al. 2018; Marino et al. 2018), with a possible contribution of the age spread (Goudfrooij et al. 2017). These results seems to suggest that MPs were formed at high redshift.

But, observing GCs with ages in range $2-10$ Gyr, populations with different N abundances have been individuated (Hollyhead et al. 2017; Niederhofer et al. 2017; Lagioia et al. 2019). This may suggest that MPs could have been formed at redshift lower than expected.

In order to characterize properly MPs, a study based on ChM is necessary. This was done by Milone et al. (2020a), analyzing 11 MCs clusters and finding

MPs in 5 of them.

Of course a comparison between galactic and extragalactic GCs is crucial to understand if and how the environment has a role on their properties. For example, Milone et al. (2020a) have found that the fraction of 1G stars in MC clusters anticorrelates with both the initial and present-day mass of the cluster, as observed for galactic GCs (Figure 1.4). Despite the fact that the small sample of extragalactic GCs avoids to understand if the two groups of clusters anticorrelates in the same way, it seems that, at similar present-day mass, MC clusters with MPs host typically larger fractions of 1G stars than Galactic ones.

1.4 Outline and purpose of the Thesis

The aim if the thesis is to give constraints on the role of formation redshift and host galaxy on the MPs phenomenon. To do so, fraction of 1G and 2G stars have been calculated for a sample of galactic and MC GCs. The outline of the thesis is the following:

- **Chapter 1.** It provides a description of the MPs phenomenon, showing its observational evidence and constraints. A brief discussion about some of the theoretical explanation of the phenomenon is then proposed. Finally, an overview of the current state of the research about the MCs cluster has been made.

- **Chapter 2.** It provides a detailed description of the instrumentation used, the sample of clusters considered and the photometric and astrometric data reduction performed on the cluster NGC 416.

- **Chapter 3.** It illustrates the data analysis and the main results of the thesis. Specifically, it includes the description of the methods used to identify the distinct populations along the rHB and derive population ratios. It provides the characterization of MPs in Galactic and extragalactic GCs and discuss some peculiar cases, including the pair of GCs NGC 6388 and NGC 6441 and the cluster NGC 6362, which is the most metal-poor analyzed cluster.

- **Chapter 4.** It investigate monovariate relations between the fraction of first-generation stars and the main parameters of the host clusters. This chapter also includes a summary of the results of the thesis and a comparison with the most recent works in literature.

Chapter 2

Data and Data Analysis

In this Chapter, I describe the data used in this work and the methods for data reduction and data analysis. The Chapter is organized as follows. Section 2.1 describes the instrumentation used to obtain the images that I analyzed in the thesis. The dataset is illustrated in Section 2.2. Section 2.3 describes the procedure to derive high-precision astrometry and photometry for the case of NGC 416. Specifically, I illustrate the method to derive accurate Point Spread Function (PSF) and measure the stars in the HST images. Section 2.4 explains the procedure used to build a catalog for each filter. Two methods are presented, one used for the bight stars and one used for the faint stars. Section 2.5 is dedicated to the calibration of the magnitudes.

2.1 Instrumentation

HST is the only telescope that nowadays can provide the high-precision photometry needed to detect and properly characterize MPs. It orbits around the Earth, avoiding distortions introduced by the atmosphere and therefore obtaining images with higher resolution than that of the majority of ground-based telescopes. Such performance is fundamental to measure accurate positions and magnitudes of stars in the crowded environment of globular clusters. Another advantage is that HST can detect photons with waveleghts that are inaccessible to ground-based telescope due to the opacity of the atmosphere, providing information in bands that are fundamental to detect and characterize MPs, including those inferred from the UV filters.

HST has a primary mirror of 2.4 m and covers a wide range of wavelenghts, from $\sim$ 100 nm to $\sim$ 1700 nm. In order to detect light in different spectral bands, the telescope has on board different cameras, each with a certain Field of View (FoV), wavelenght range and plate scale (ps). The images used in this work have been obtained with the two following cameras:

- **Advanced Camera for Surveys (ACS).** It has three channels:
  - High Resolution Channel (HRC), with $FoV = 29.1 \times 26.1\ arcsec^2$, covering a wavelenght range of $200 - 1050\ nm$ and with $ps = 0.027\ arcsec\ pixel^{-1}$.

Table 2.1: Summary of the information about all the images used in the photometric data reduction of NGC 416.

DATE	N× EXPTIME	FILTER	INSTRUMENT	PROGRAM	PI
2019 Jun 18	1500s+1512s+2×1529s+2×1525s	F275W	UVIS/WFC3	15630	N. Bastian
2019 Jul 31	1530s+1500s+2×1533s+2×1534s	F275W	UVIS/WFC3	15630	N. Bastian
2019 Aug 05	2×1500s+1512s+2×1515s+1523s	F275W	UVIS/WFC3	15630	N. Bastian
2016 Jun 16	700s+1160s+1200s	F336W	UVIS/WFC3	14069	N. Bastian
2016 Jun 16	500s+800s+1650s+1655s	F343N	UVIS/WFC3	14069	N. Bastian
2016 Jun 16	75s+150s+440s+460s	F438W	UVIS/WFC3	14069	N. Bastian
2005 Nov 22	2×20s	F555W	WFC/ACS	10396	J. Gallagher
2006 Mar 08	2×20s+4×496s	F555W	WFC/ACS	10396	J. Gallagher
2005 Nov 22	2×10s+4×474s	F814W	WFC/ACS	10396	J. Gallagher
2006 Mar 08	2×10s+4×474s	F814W	WFC/ACS	10396	J. Gallagher

  - Solar Blind Channel (SBC), with $FoV = 34.59 \times 30.8\ arcsec^2$, covering a wavelenght range of $115 - 180\ nm$ and with $ps = 0.032\ arcsec\ pixel^{-1}$.
  - Wide Field Channel (WFC), with $FoV = 202 \times 202\ arcsec^2$, covering a wavelenght range of $350 - 1050\ nm$ and with $ps = 0.05\ arcsec\ pixel^{-1}$.

- **Wide Field Camera 3 (WFC3).** It has two channels:
  - UVIS, for ultraviolect and visible light, with $FoV = 160 \times 160\ arcsec^2$, covering a wavelenght range of $200 - 1000\ nm$ and with $ps = 0.04\ arcsec\ pixel^{-1}$.
  - NIR, for near infrared light, with $FoV = 123 \times 137\ arcsec^2$, covering a wavelenght range of $850-1700\ nm$ and with $ps = 0.13\ arcsec\ pixel^{-1}$.

2.2 Dataset

In this work I investigate multiple populations in 13 Galactic GCs, namely NGC 104 (47 Tuc), NGC 5927, NGC 6304, NGC 6352, NGC 6362, NGC 6366, NGC 6388, NGC 6441, NGC 6496, NGC 6624, NGC 6637, NGC 6652 and NGC 6838. For these clusters, we used the astrometric and photometric catalogs by Milone et al. (2017) and Anderson et al. (2008), who provide differential-reddening corrected photometry of stars in the central field of each cluster in the $F275W$, $F336W$, $F438W$ filters of WFC3/UVIS and the $F606W$ and $F814W$ filters of ACS/WFC.

To analyze the LMC cluster NGC 1978 we exploited the catalogs by Lagioia et al. (2019), who provide differential-reddening corrected photometry of stars in the central field of each cluster in the $F275W$, $F336W$, $F343N$, $F438W$ filters of WFC3/UVIS and the $F555W$ and $F814W$ filters of ACS/WFC.

Astrometry and photometry of NGC416 of the SMC has been carried out in this work. The main properties of the images used in this work are summarized in Table 2.1, while the data reduction is described in the following.

2.3 Effective Point Spread Function Photometry

The procedure described in this Section is applied for each image of NGC 416. The aim of this process is to obtain accurate measurements of position and magnitude of its stars.

2.3.1 The effective Point Spread Function

As explained in Anderson & King (2000), in a typical HST image of a GC, stars appear as relatively isolated point-like sources. In order to describe them, only three parameters are necessary: the center coordinates (x, y) and the total flux (f). Deriving these parameters, starting from the 2-dimensional pixel array that is the image, is a crucial target for an high precision photometry.

Finding out accurate positions requires an accurate PSF model. Inaccuracies can lead to systematic errors in stars position measurements, as shown in Figure 2.1. The bias induced, called pixel-phase error, depends on the location of the star within the pixel. The same stellar profile can be fitted with different PSF models. Without knowing a-priori the stellar position, which is obviously impossible, one cannot identify an accurate PSF.

To solve this issue, it is important the following consideration. The two-dimensional PSF describes how the light of a point-like source (as a star in a GC) is distributed after being processed by a telescope. Each star image is a replica of the PSF, with certain values of position and flux. The PSF produced by a telescope at its focal plane is called intstumental PSF (iPSF). But it is impossible to observe it directly, what can actually be observed is an array of pixels, each one with a value of registered counts. A star image is distributed over several pixels. The value of counts in a pixel centered at some offset $(\Delta x, \Delta y)$ from the center of the iPSF, depends on the results of a convolution between the iPSF and the sensitivity profile of a pixel.

The effective PSF (ePSF), as defined in Anderson & King (2000), is this convolution. It gives directly the fraction of a star light that should fall in each pixel of a star image, taking account of where the center of that pixel lies with respect to the center of the star. The ePSF is a continuous function and it is smoother than the iPSF.

The ePSF has three major advantages with respect to the iPSF. First of all, ePSF simplifies the calculations: fitting it to a stellar image does not require an integration, but only to adjust the values of centre coordinates and total flux until the sum of the squares of the residuals is minimized. The second advantage is that it is easier to solve for an ePSF. Knowing x, y and f of a certain pixel, one can derive at which offset $(\Delta x, \Delta y)$ a certain pixel has sampled the ePSF. If the 3 values are known for a large number of pixels, it is possible to obtain a very large number of estimates of ePSF in function of $(\Delta x, \Delta y)$. The third one regards the fact that the values of ePSF result from an integration over the actual pixel sensitivity profile of the detector, thus no assumption about sensitivity variations within a pixel is necessary. It represents whatever results from the combination of the detector and iPSF, without assuming anything about any of them.

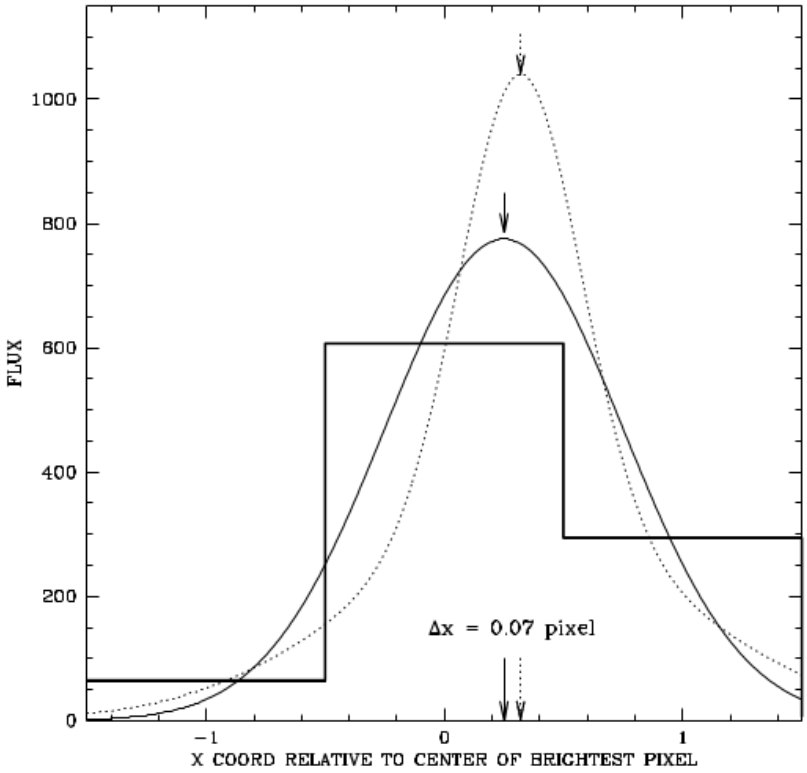

Figure 2.1: The histogram shows the flux value in three adjacent pixels. The two smooth curves represent two different PSF model, which give different peak (and therefore center) positions (Anderson & King 2000).

2.3.2 Deriving the effective Point Spread Function Model for NGC 416

The techniques presented in Section 2.3.1 are here applied to derive a PSF model for the stars in each exposure of NGC 416. In theory, to derive an appropriate PSF model we would need stellar position and fluxes, but no positions and fluxes can be measured without a PSF model. To break this degeneracy we adopted an iterative procedure. As a first step, we used a library PSF suitable for the filter and the camera to estimate first-guess positions and magnitudes[1]. Such raw quantities are used to derive an improved PSF model that we used to measure stars in the next iteration.

An iteration is a procedure that consists in three stages. At first, raw positions and magnitudes of each pixel near a star are converted into an estimate of ePSF in the corresponding point. Then, the measured ePSF is used to better es-

[1]Actually, no library PSF model is available for the $F343N$ filter. Hence, we used a library PSF derived from $F336W$ images, which is similar to the $F343N$ PSF. I emphasize that such library PSF is adopted to derive the first-guess positions and magnitudes of stars that we used to derive the appropriate ePSF model by using the iterative procedure described in Section 2.3.2.

timate, by least-square fitting, position and magnitude of each star considered. Finally, the values found in the previous stage are transferred in a common reference frame, combining them and analyzing the residuals. However, there is still a problem regarding the degeneracy between the model and the center position of a star. The bias introduced by the pixel-phase error can be avoided considering multiple observations of the same star at different dither positions. Averaging the multiple observations makes possible to obtain a better ePSF profile. These stages are repeated iteratively, improving the model until it basically does not change anymore between two subsequently iterations.

The first iteration allows to build a model based on the actual image, using the raw positions and magnitudes obtained from fitting the PSF library. To do so, the most isolated and luminous (but not saturated) stars not contaminated by cosmic rays have been considered. This was done using the two fortran routines `jena_img2psf` (Anderson & King 2000), one for exposures taken with WFC3 and one for exposures taken with ACS. These routines find all the stars in a certain image that meet some criteria, defined by the following arguments:

- **HMIN.** It defines the minimum distance (in pixels) that two sources can have to be considered. A typical value here used is 11.
- **FMIN.** It defines the minimum counts value that a source can have to be considered. A typical value here used is 2000.
- **PMAX.** It defines the maximum counts value that a source can have to be considered. A typical value here used is 54900 (right below the saturation limit).
- **QMAX.** It defines the maximum value of the Q parameter, an indicator of the quality of the fit. If it is too high, the source fitted is probably not a star. A typical value here used is 0.3.
- **NSIDES.** It defines in how many regions the image has to be divided. Using a lot of different regions helps to take account of variations of the PSF across the chip. The value is kept at 1 for all the images analysed.
- **PSFFILE.** It defines what initial PSF model is used.
- **IMG.fits.** It defines the image on which the procedure is performed.

Then another routine, `img2xym` (Anderson & King 2006), has been utilized. It uses the just derived PSF model to obtain positions and magnitudes of all the sources that satisfy some criteria, defined by the values of HMIN, FMIN and PMAX, in a given image. This time a larger number of stars is considered, imposing $HMIN = 5$, $FMIN = 50$ and $PMAX = 9999$.

This procedure has to take account that, because of position-dependent charge diffusion and optical aberrations, the PSF could change shape by changing position on the detector. For this reason the software used do not compute a single PSF, but a grid of 9×10 PSFs. An example is given in Figure 2.2, where in left panel is represented an exposure of NGC 416 and in the right panel is shown the respective PSF grid derived. The PSF model for any point in the detector is then obtained by interpolating the PSF among the four nearest grid points.

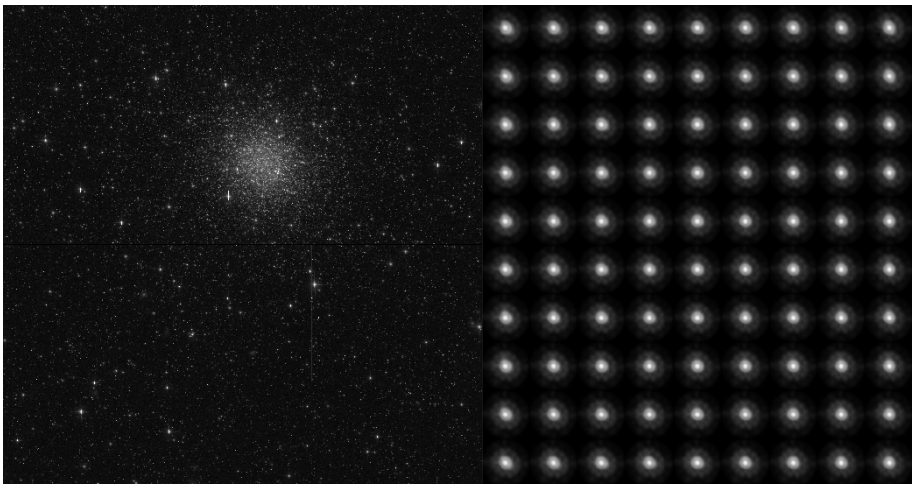

Figure 2.2: Images of an exposure of NGC 416 with filter F814W (at left) and of the respective iPSF model obtained (at right).

The procedure is applied for each image in each filter, resulting in a group of files containing, among other quantities, positions and instrumental magnitudes (given by $m = -2.5 \log f$).

2.4 Building the Catalog

Once derived position and magnitude of each star in all the images, it is possible to build a catalog of stars in NGC 416. The images can be reduced through two different methods, which use different approaches. In the first one, presented in Section 2.4.1, every image is reduced singularly. Then, for each filter the information on all the images is put together. In the second one, presented in Section 2.4.2, images in each filter are stacked in a single images. Then, these images are reduced. The first method gives more accurate positions and magnitudes than the second for bright stars, while the second gives more accurate results for faint stars. Therefore, a combination of the two methods is necessary in order to obtain photometry of the best possible accuracy.

2.4.1 Bright Star Analysis

The files obtained in Section 2.3.2 contain sources that fulfilled all the requirements inserted in the routines, but not all are real stars. In order to delete from the catalog these unwanted sources, it is important to consider the value of Q. This parameter, as said before, is a good indicator of the quality of the fit, telling how much the PSF reproduces a source. The well-reproduced sources are stars. For those ones, Q has a defined dependence from magnitude, being smaller if the source is brighter. Thus, a sort of cleaning process is necessary, as explained in Figure 2.3, keeping only the blue stars. During this process, it is important to not clear saturated stars, because they are necessary in next operations. Therefore, the cleaning is only made for stars with $m > -13.7 mag$.

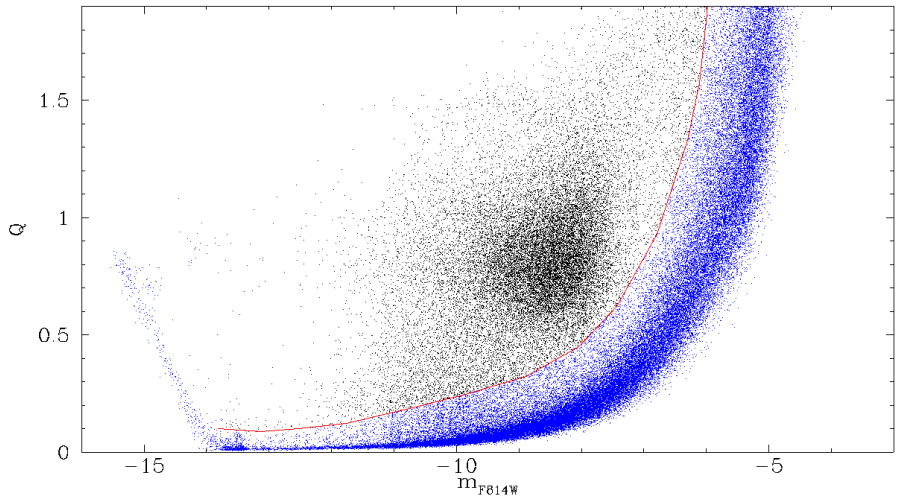

Figure 2.3: Cleaning process for stars in one F814W exposure. The red line separates the good stars (in blue) and the discarded stars (in black).

The next step is to obtain catalogs for all 6 filters. To do so, a master for each one has been chosen, that is an image used as reference frame. This is necessary because the different images are not perfectly superimposed. In order to bring each one in the master reference frame, it is used the routine `xym2mat`, developed by Jay Anderson. Its aim is to identify the same stars in different images, through two iterations.

In the first one, the brightest stars of the master and in other images (considering also the saturated ones) are identified. The routine starts now to look for triangles of stars with similar sides ratio between the master and the analysed image. By finding these triangles, common stars can be identified. Using the coordinates of this group of stars in both master and image reference frame, it calculates, by least square fitting, the 6 coefficients of the linear transformation that allows to change coordinates:

$$\begin{cases} x_1 = A + Cx_2 + Ey_2 \\ y_1 = B + Dx_2 + Fy_2, \end{cases} \tag{2.1}$$

where A, B, C, D, E and F are the coefficients, while (x_1, y_1) and (x_2, y_2) are the coordinates of a star in the two reference frames.

Therefore, positions and magnitudes of each image can be expressed in terms of the master reference frame. But the saturated stars are not well measured, so in building an accurate catalog they should not be taken into account. In fact, a second iteration is performed considering only not saturated stars, starting from the transformation derived in the first one. What is obtained in the procedure is a series of files with position and magnitude of the common stars and their residuals with respect to the master. A distribution of the residual of the position is shown in Figure 2.4. The `xym2mat` routine requires one argument, that is the distance (in pixels) from a star within which the program search for common stars. In the first iteration the distance is kept quite large, while in the second one is smaller.

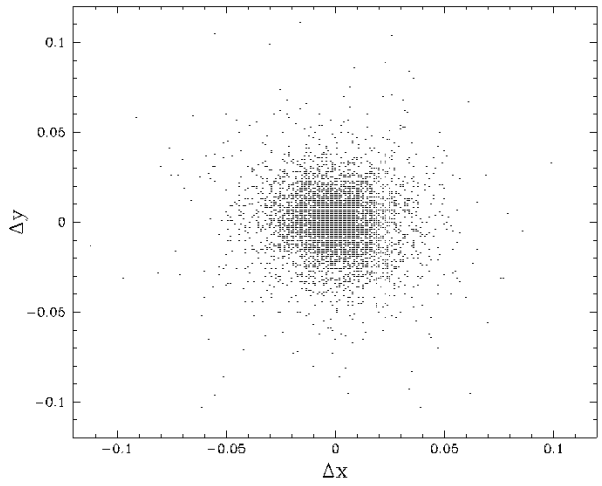

Figure 2.4: Plot of the residuals of the transformation between the master and an other image for filter F336W.

After that, it is possible to obtain a catalog for each filter, using the routine `xym2bar`, developed by Jay Anderson. It calculates the average values of position and magnitude between the common stars. One argument is required, that is the minimum number or different images in which the same star has to be individuated to be considered. It comes from a compromise between having catalogs with a large number of stars or with a few better measured stars, and depends of course on the number of images available for a given filter. On building these files, all the stars brighter than -5 *mag* have been considered, avoiding the fainter ones. This is due to the fact that this part of photometric reduction works better for bright stars, while the faints will be analyzed in Section 2.3.4.

The next step is to obtain catalogs with stars magnitude in different filters. To do so, the routine `xym1mat`, developed by Jay Anderson, has been used to link catalogs together. Once chosen a reference catalog (or master), the software is used to link it with the ones in other filters, finding the corresponding stars (which are not necessarily in the same order in different catalogs). The master here used is the catalog in F814W.

The last thing done in this part of data reduction consists in expressing the stars coordinate with respect to an absolute reference frame, that is the GAIA one. First of all, the catalog of NGC 416 has been downloaded from the GAIA Data Release 1 (DR1; Gaia Collaboration et al. 2016a, 2016b).[2] Since positions from DR1 are expressed in terms of right ascension (RA) and declination (DEC), it has been necessary to transform them in linear coordinates. Then, using again `xym1mat`, the previously obtained catalog in F814W is linked with the GAIA one. A new master frame is now created, with GAIA positions and HST magnitudes. Starting from this one, the `xym2mat` and `xym2bar` procedure is now repeated, obtaining a new F814W catalog. For the other filters, which will be linked to the F814W, the just got catalog and the one in the designed filter have been tied up

[2]The data here used can be consulted on the website `https://gea.esac.esa.int/archive/`.

together using `xym1mat` routine. The master frame in each filter is then given by the GAIA positions and the HST magnitudes. Finally, the `xym2mat` and `xym2bar` procedure is now repeated, obtaining a new catalog for each filter. Of course, all these new catalogs have been linked to the F814W one with `xym1mat`.

2.4.2 Faint Stars Analysis

As already mentioned in the beginning of this Section, the data reduction accomplished so far is very accurate for bright stars, but not so much with faint stars, that require multiple detections in different exposures to be found and measured. It is for that used the routine `KS2` (Anderson et al. 2008; Nardiello et al. 2018). It requires the files containing information about the transformations into the master reference frame and a PSF model for each image in each filter, both obtained in the previous operations.

`KS2` analyses all the images at the same time, giving strong advantage in finding and measuring the faint stars, characterized by low signal-to-noise ratio. No saturated stars are measured by the software, that creates a mask for covering them, in order to measure also their nearby stars.

The finding procedure is iterative: 9 iterations are performed, each one with different imposed criteria. In the first one, the routine identifies the brighter stars and subtracts them. In the subsequent iterations, progressively fainter stars are searched. Among the various outputs given by the software, three astrometric and photometric catalogues of stars are generated by using three different methods.

Method 1 gives its best results with the brighter stars, which are able to generate star-like profiles in a single exposure. The final values of position and magnitude of a star in each filter comes from the average of the measurements in single exposures.

Method 2 gives its best results for faint stars and in crowded fields. `KS2` performs weighted aperture photometry of the stars, in the sense that pixel containing neighbour stars are down-weighted.

Method 3 gives its best in very crowded fields. It operates similarly to method 2, with the difference that considers only pixels within a radius of 0.75 pixels from the star centre.

The m_{F275W} vs $m_{F275W} - m_{F814W}$ CMD are represented in Figure 2.5. I can be seen in its three panels that method 1 provides more accurate photometry for bright stars, while method 2 and 3 provide better estimates for the faintest stars in the diagram.

The routine also generates stacked images, one for each defined slot. The slots are group of images separated by filter and, when necessary, by long and short exposure times. The images have been divided into 10 slots, therefore 10 stacked images are obtained for NGC 416.

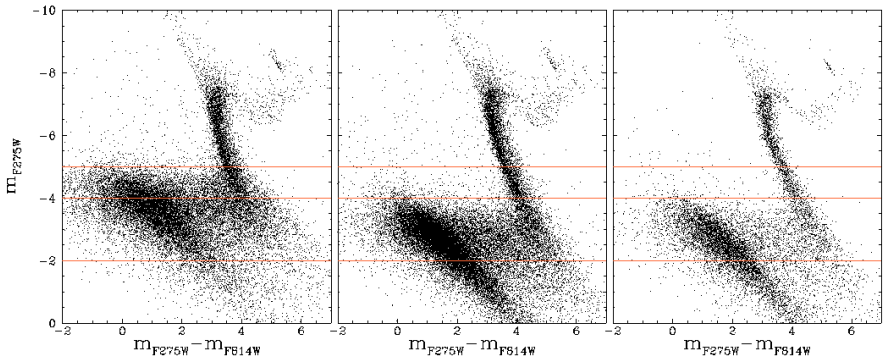

Figure 2.5: CMDs derived from the three methods: method 1 at left, method 2 at the centre and method 3 at right. Three orange horizontal lines are drawn, helping to show that at $m_{F275W} > -5$, thus for faint stars, methods 2 and 3 provide better measurements.

2.5 Calibration

In order to have a physical meaning, instrumental magnitudes need to be calibrated. The calibrated magnitude is given by the relation

$$m_{cal} = m_{inst} + \Delta mag + ZP_{filt} + C, \tag{2.2}$$

where m_{instr} is the instrumental magnitude, Δmag is the difference between PSF and aperture photometry, ZP_{filt} is the zero-point for a given filter and C is the aperture correction.

In order to find Δmag, the routine `drz_phot_gfortran` has been used. It measures the aperture magnitudes in the images in drz format, which are images of NGC 416 at an exposure time of 1 s, thus with the values registered in each pixel that are actually the number of counts per unit second. It needs the following arguments: isolation index (HMIN), minimum and maximum flux (respectively FMIN and PMAX) and the image analysed. The arguments are defined with the aim of considering only bright, isolated and not saturated stars. In order to perform the aperture photometry, aperture radius, inner and outer radius have been defined. They have been chosen to be as large as possible, without including the flux of other nearby sources.

The aperture magnitudes are then utilized to estimate Δmag. The procedure is iterative: plotting Δmag vs m_{instr} (obtained from PSF photometry) and considering the brightest and better measured stars, one can find an average value of Δmag. In the first iteration, an initial by-eye value of Δmag and an interval around it of 4-5 σ (also this one imposed arbitrarily) have been used to select an initial sample of stars. Then, the Δmag median and the σ of the selected stars is calculated. Using this values as the initial ones, the procedure is repeated considering stars within an interval of 2-3 σ, until the result does not change between two subsequent iterations. The final result of these iterations is shown in Figure 2.6.

The values of ZP_{filt} and C can be found from the utility available at `http://www.stsci.edu/hst/instrumentation/wfc3/calibration` for observation

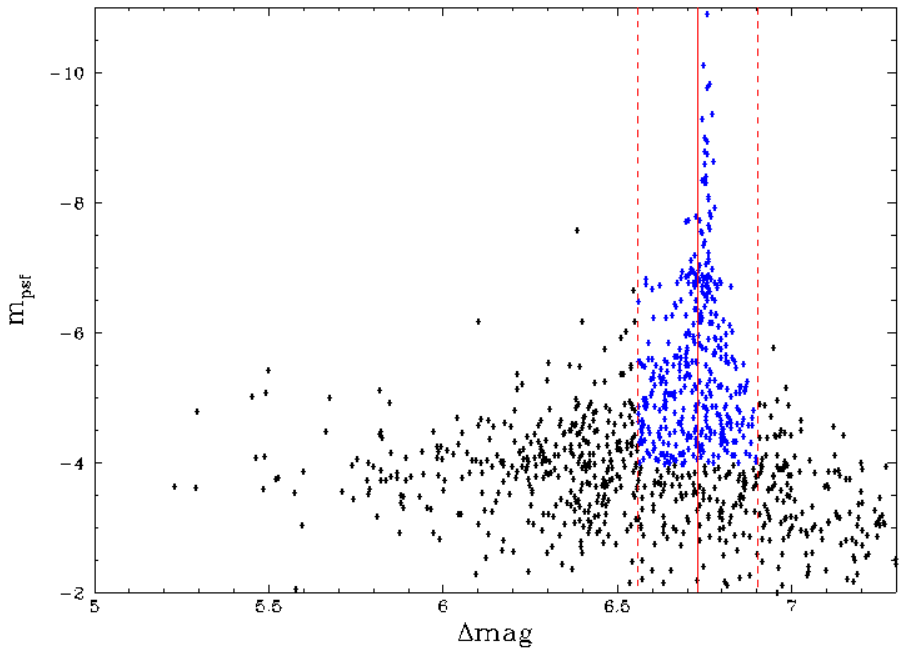

Figure 2.6: Plot of the instrumental magnitude (from PSF photometry) with respect to Δmag, used to find the latter one. the red vertical continuous line indicates the value of Δmag found from the iterative procedure an the dashed are located at a distance 2σ from the central one. The blue stars are the ones used to estimate the median.

with WFC3 and at `http://www.stsci.edu/hst/acs/analysis/zeropoints` for observations in ACS. These values depend on the filter considered, the date of observation and the aperture radius.

Chapter 3

Results

In this Chapter I analyze the photometric and astrometric catalogs derived in the previous Sections to identify and characterize the MPs of fifteen Galactic and extragalactic GCs. To do this, I exploit, for the first time, the red HB. The Chapter is organized as follows. Section 3.1 describes the procedure adopted to correct the effect of differential reddening on the photometry. Section 3.2 presents the method to estimate of the fraction of 1G and 2G stars among the red HB, while Section 3.3 shows in details the diagram used to separate different populations in rHB. Section 3.4 describes the peculiar case of NGC 6362. The GCs NGC 6388 and NGC 6441, which are considered 'twin' GCs, are compared in Section 3.5.

3.1 Differential Reddening Correction

The presence of molecular clouds and interstellar dust causes an absorption of the light emitted from an astronomical object. This absorption is a function of radiation frequence, and it is larger at smaller wavelenghts (λ). Considering observations in a given band X, the difference between the apparent magnitude (m_X) and the original magnitude (m_0) is the quantity

$$A_X = m_X - m_0, \tag{3.1}$$

called interstellar absorption. The difference between the apparent magnitude of a star in a band X_1 and X_2 with $\lambda_{X1} < \lambda_{X2}$ is expressed by the so called color excess

$$E(X_1 - X_2) = A_{X1} - A_{X2}, \tag{3.2}$$

It indicates the difference between the apparent colour and the original colour of a star. If $X_1 = B$ and $X_2 = V$, this quantity is called reddening. A relation between A_X and $E(B-V)$ is given by

$$A_X = k_X E(B-V). \tag{3.3}$$

The k_X values for the filters of HST used in this work are $k_{F275W} = 6.3828$, $k_{F336W} = 5.1002$, $k_{F343N} = 4.9946$, $k_{F438W} = 4.1818$, $k_{F555W} = 3.2118$, $k_{F606W} = 2.8782$ and $k_{F814W} = 1.8420$.

The interstellar reddening is not constant, but changes with the direction of the line of sight. When we observe a GC, small differences of $E(B-V)$ across the Field of View (FoV) of an observation, referred as differential reddening (DR), produce an artificial spread in a typical evolutionary sequences of the CMDs. As a consequence, DR can dramatically reduce the amount of information of the properties of stellar populations of a cluster that we can infer photometrically. In order to minimise the impact of DR on our photometry, we adopted the procedure for DR correction introduced by Milone et al. (2012b).

This method is explained in Figure 3.1, using NGC 2298 as a template. Panel (a) displays the m_{F606W} vs $(m_{F606W}-m_{F814W})$ CMD, where cluster stars are plotted as grey points. The red arrow represents the reddening vector and defines a new reference system, where the "abscissa" is parallel to the reddening vector direction and the "ordinate" is perpendicular to it. The two dotted lines define a subsample of cluster stars (black points) used for the computation of the DR. In panel (b) the selected stars are represented in the new reference system. The dashed red line marks the fiducial line of the cluster stars. This fiducial line is obtained by dividing the interested region of the CMD in small magnitude bins and interpolating the values of the median of the colour and magnitude of stars in each bin. Panel (c) displays the difference between the colour of each star and that of the fiducial line, Δ "abscissa". The subsample of stars used is located in a region of the CMD where the angular separation between the evolutionary sequence and the direction of the reddening vector is maximum. In this portion of the CMD, indeed, the impact that the random magnitude errors has on the observed colour spread is minimum when compared with the effect of DR.

Then, the DR value of each cluster stars is estimated as the median value of the Δ "abscissa" scatter of the 30–100 closest spatial neighbour star. This quantity is an estimate of the DR that affects that star.

This procedure is applied to all the cluster studied in the thesis. As an example, the two-panel Figure 3.2 compares the m_{F275W} vs. $m_{F275W}-m_{F814W}$ CMD of the Small Magellanic Cloud cluster NGC 416 before (left) and after (right) applying the DR correction. We observe that the color width of the RGB in the right CMD, equal to $\sim 0.8\ mag$, is significantly reduced in the DR-corrected left CMD, where it is equal to $\sim 0.4\ mag$. We also observe a significant reduction of the colour and magnitude of the cluster HB stars, which appears more defined in the DR-corrected CMD. Finally we see that the RGB bump, barely visible in the original CMD, is clearly visible in the DR-corrected CMD as an overdensity of stars at $m_{F275W}-m_{F814W} \sim 4.2\ mag$ and $m_{F275W} \sim 21\ mag$.

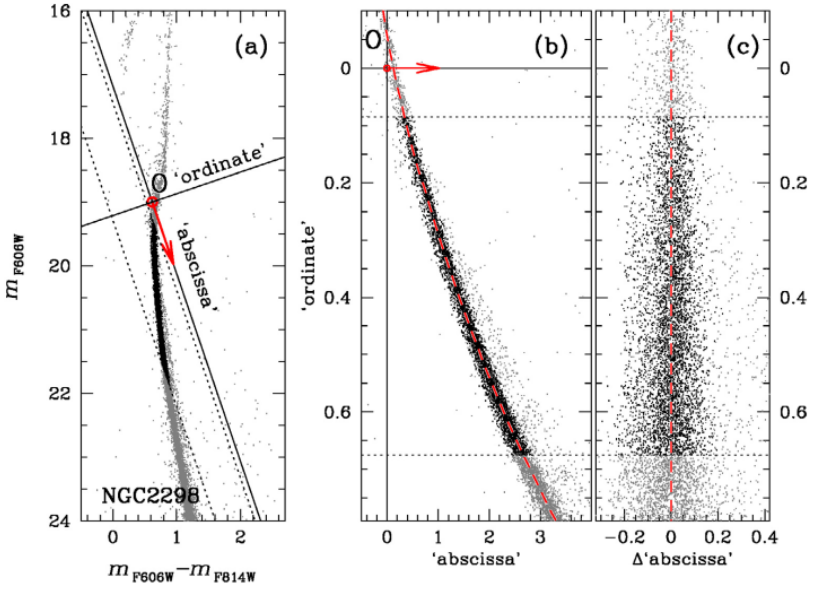

Figure 3.1: This figure illustrates the method for the correction of differential reddening in the photometry of NGC2298 (from Milone et al. 2012c). The red arrow in panel (a) indicates the direction of reddening. The continuous black lines are "abscissa" and "ordinate" of the reference frame introduced in the procedure. The dotted lines define an interval within which the subsample of stars is selected. The position of NGC 2298 stars in this reference frame is shown in panel (b) where the fiducial line of the MS is drawn as a dashed red line. Panel (c) shows the "ordinate" vs. Δ "abscissa" diagram.

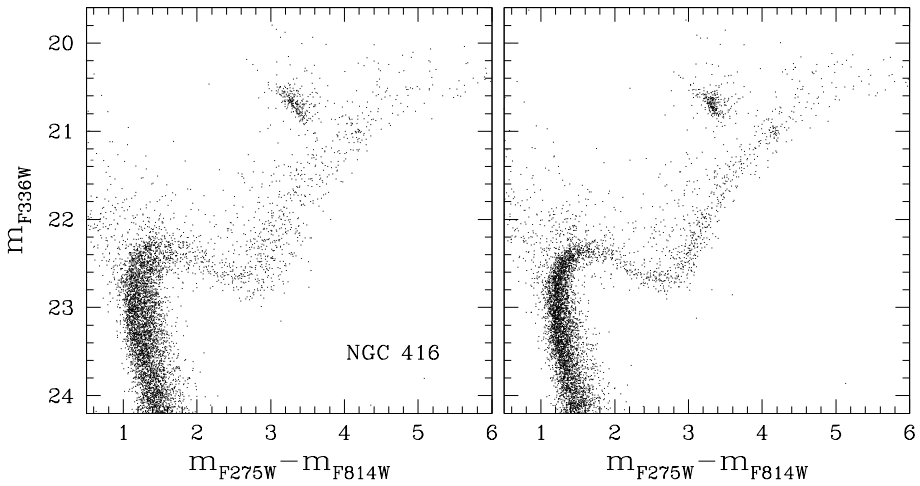

Figure 3.2: m_{F275W} vs. $m_{F275W} - m_{F814W}$ CMD of the Small Magellanic Cloud cluster NGC 416 before (left panel) and after (right panel) applying the differential reddening correction.

3.2 Population ratio from the red HB

To identify 1G and 2G stars along the red HB of each cluster, and measure the fraction of stars in each population, we extended to the fifteen analyzed GCs, the recipe introduced by Milone et al. (2012d) in their study of 47 Tuc.

The procedure is illustrate in Figure 3.3, where we used NGC 6388 as a template, and it was performed through the following steps:

1. **Selection of HB stars.** I identify by eye the cluster HB stars in the m_{F438W} vs $m_{F438W} - m_{F814W}$ CMD, plotted in the upper panel of Figure 3.3. The red HB (rHB) stars, which are the coldest HB members are plotted with black points, whereas the remaining HB stars correspond to the blue HB (bHB) and are represented with blue crosses.

2. **Two-colour diagram and selection.** The lower-left panel of Figure 3.3 displays the $m_{F275W} - m_{F336W}$ vs $m_{F336W} - m_{F438W}$ two-colour diagram of HB stars, zoomed on the rHB. The observed distribution shows two main distinct groups of rHB stars, distributed in two approximately parallel sequences aligned along the top-left–bottom-right direction. Specifically, the sequence of 1G stars exhibit redder $m_{F275W} - m_{F336W}$ colors than 2G stars with the same $m_{F336W} - m_{F438W}$. The dot-dashed lines empirically separates the bulk of 1G stars from the remaining HB stars, which belong to the 2G. The reason why the adopted two-colour diagram, which is based on the F275W, F336W, and F438W, is a powerful tool to identify multiple populations along the rHB is quite simple (Milone et al. 2012d). Indeed, the F275W passband includes an OH molecular band, F336W an NH band, and F438W CN and CH bands. The relatively-cold 1G stars, which are oxygen- and carbon-rich and nitrogen-poor, are relatively faint in F275W and F438W, but bright in F336W. On the contrary, rHB 2G stars, whose material has been CNO-cycle processed, are oxygen- and carbon-poor but nitrogen-rich. As a consequence, they are relatively bright in F275W and F438W but faint in F336W. Therefore, 1G stars are bluer than 2G stars in (F336W−F438W), but redder in another (F275W−F336W). Hence, 1G and 2G stars define distinct sequences in the $m_{F275W} - m_{F336W}$ vs $m_{F336W} - m_{F438W}$ two-colour diagram.

3. **Verticalized two-colour diagram.** In the lower-middle panel of 3.3, I plotted the $m_{F275W} - m_{F336W}$ vs $\Delta(m_{F336W} - m_{F438W})$ diagram, where the last quantity represents the difference between the $m_{F336W} - m_{F438W}$ of the rHB stars and that of the fiducial line at the corresponding $m_{F275W} - m_{F336W}$ colour. In this diagram, the two sub-groups are now distributed vertically.

4. **Building the histogram.** The lower-right panel shows the histogram distribution of $\Delta(m_{F336W} - m_{F438W})$ for rHB stars, obtained by using a bin-width = 0.015 *mag*. The histogram shows two peaks: the primary at $\Delta(m_{F336W} - m_{F438W}) \sim 0.1$ *mag* and the secondary at $\Delta(m_{F336W} - m_{F438W}) \sim -0.1$ *mag*.

5. **Measuring the fraction of 1G stars in among the rHB.** I used a bi-Gaussian function to fit the histogram distribution of $\Delta(m_{F336W} - m_{F438W})$ by means of least squares. The best-fit function is represented

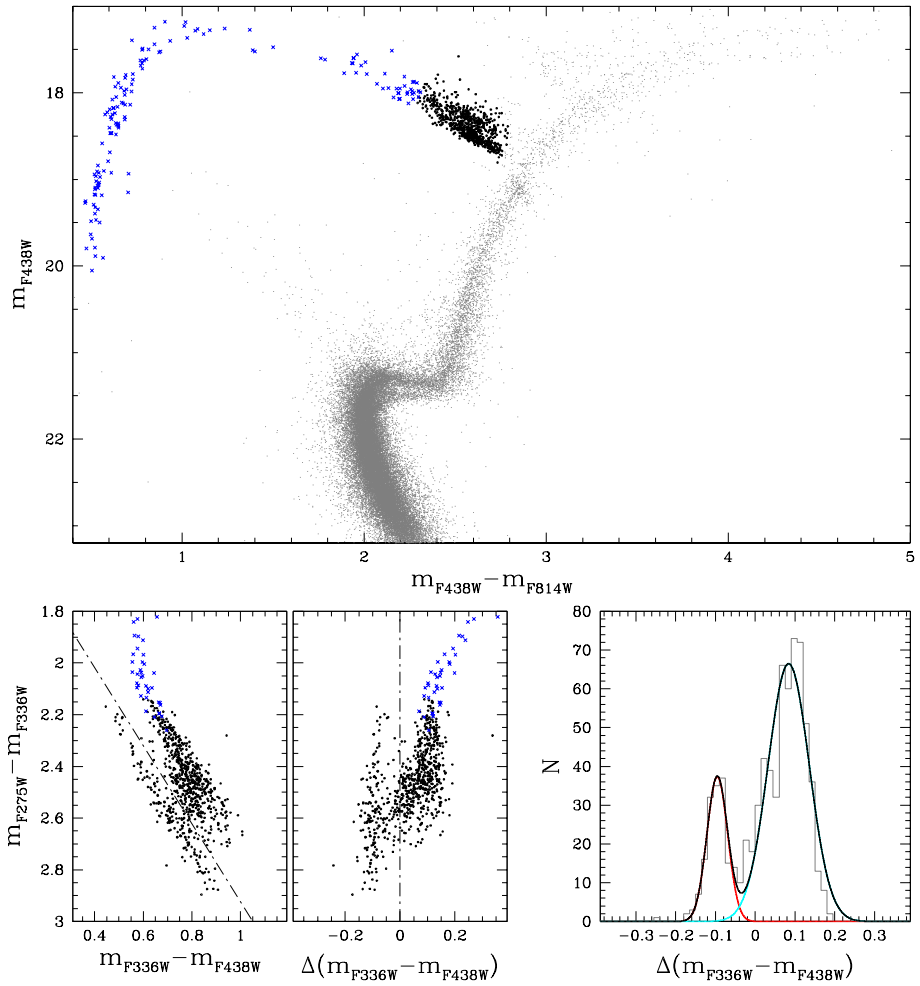

Figure 3.3: Method for the estimate of the fraction of 1G and 2G stars from HB stars. In the upper panel is represented the CMD of NGC 6388, with the rHB stars in black and the bHB stars in blue. In the lower left panel, the two-colour diagram of the rHB stars is shown. The dot-dashed black line has been drawn by-eye in order to obtain the diagram in lower central panel, where the difference between the line and the $m_{F336W} - m_{F438W}$ value of each star is plotted, that is $\Delta(m_{F336W} - m_{F438W})$. In this way, it is obtained a verticalized diagram, which makes possible to plot the histogram shown in lower right panel. In grey the number of stars in each bin of $\Delta(m_{F336W} - m_{F438W})$ is represented, in red the Gaussian function used to fit the 1G stars and in cyan the one used to fit the 2G stars. The black curve is the sum of two Gaussian functions.

with the black line superimposed on the histograms plotted in the bottom-right panel of Figure 3.3, while the two Gaussian components corresponding to the 1G and the 2G are colored red and cyan, respectively. The fraction of 1G stars among the red HB is then evaluated as the ratio between the area subtended by the red Gaussian and the area subtended by the black curve. Specifically, the number of 1G stars in the rHB is

$$(N_{1G})_{rHB} = \frac{Area\ subtended\ by\ red\ gaussian}{Area\ subtended\ by\ black\ function.}(N_{TOT})_{rHB} \quad (3.4)$$

where $(N_{TOT})_{rHB}$ is the total number of stars in red HB.

Most of the analyzed GCs do not host bHB stars. Hence, the fraction of 1G stars among the red HB correspond to the total fraction of 1G stars. To derive the fraction of 1G stars in NGC 6388 and NGC 6441 we must account for the presence of the bHB, which is composed of 2G stars alone (e.g. Marino et al. 2011, 2014). In these cases, indicating $N_{TOT} = (N_{1G})_{rHB} + (N_{2G})_{rHB} + (N_{2G})_{bHB}$, the fraction of 1G stars corresponds to:

$$\frac{N_{1G}}{N_{TOT}} = \frac{(N_{1G})_{rHB}}{N_{TOT}} \quad (3.5)$$

3.3 Multiple populations along the red HB

The procedure described in the previous Section has been extended to all Galactic GCs to distinguish 1G and 2G stars along the red HB and derive the population ratios.

Results are summarized in Figure 3.4, where I display the collection of $m_{F275W} - m_{F336W}$ vs $m_{F336W} - m_{F438W}$ two-colour diagrams of the rHB stars of all the analyzed Galactic clusters. Figure 3.5 shows the corresponding $m_{\rm F336W}$ vs. $C_{F275W,F336W,F438W} = (m_{F275W} - m_{F336W}) - (m_{F336W} - m_{F438W})$ diagrams, where I marked in red the 1G stars selected with the method described in the previous Section. For completeness, we show in Figure 3.6 the $m_{\rm F438W}$ vs. $m_{\rm F438W} - m_{\rm F814W}$ CMDs of the analyzed clusters. Interestingly, 1G stars are redder and fainter than the bulk of 2G stars in these optical colours and magnitudes. This fact corroborates the evidence that 2G stars are enhanced in helium with respect to the 1G.

Clearly, the distribution of 1G and 2G stars in the $m_{F275W} - m_{F336W}$ vs $m_{F336W} - m_{F438W}$ and $m_{\rm F336W}$ vs. $C_{F275W,F336W,F438W}$ exhibit a large degree of variety, with the relative numbers of 1G and 2G stars, as well as the extension of 1G and 2G sequences of rHB stars, dramatically changing from one cluster to another. Specifically, the fractions of 1G stars in the studied Galactic GCs range from ∼15%, in the case of NGC 6388 to ∼68% in NGC 6838. The results are listed in Table 4.1.

3.3.1 A new tool to disentangle multiple populations along the red HB

In addition to F275W, F336W and F438W data, in the case of 47 Tuc, images in F343N are also available. As shown by Milone et al. (2020a), the

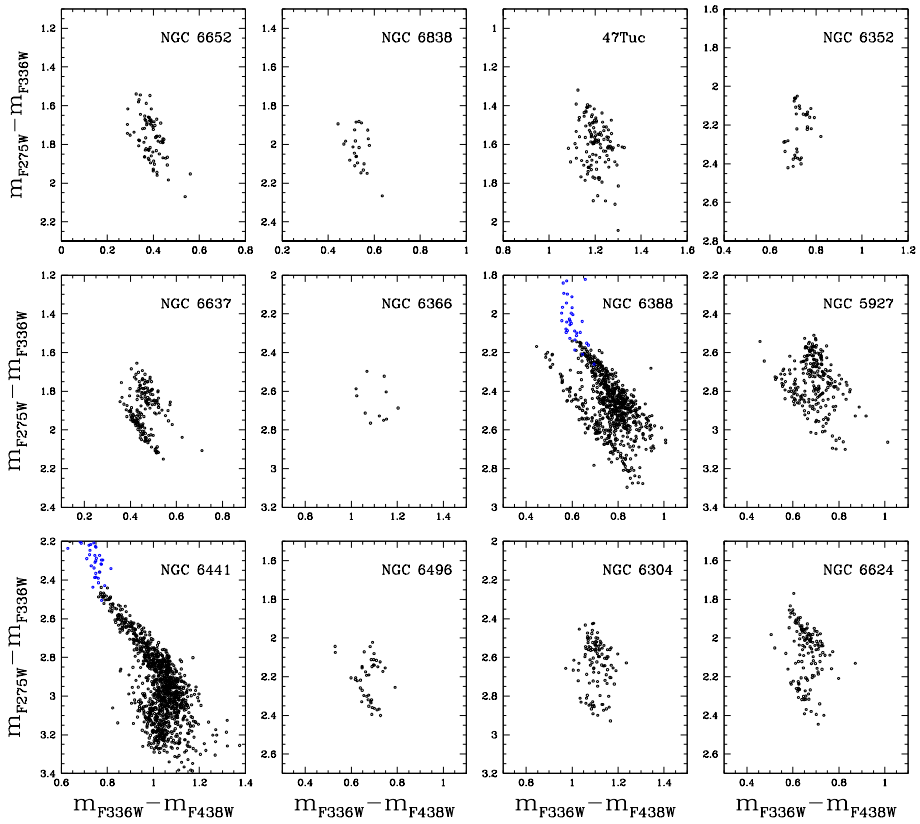

Figure 3.4: $m_{F275W} - m_{F336W}$ vs $m_{F336W} - m_{F438W}$ two-colour diagrams of the rHB of the analyzed Galactic GCs. Blue crosses mark bHB stars of NGC 6388 and NGC 6441.

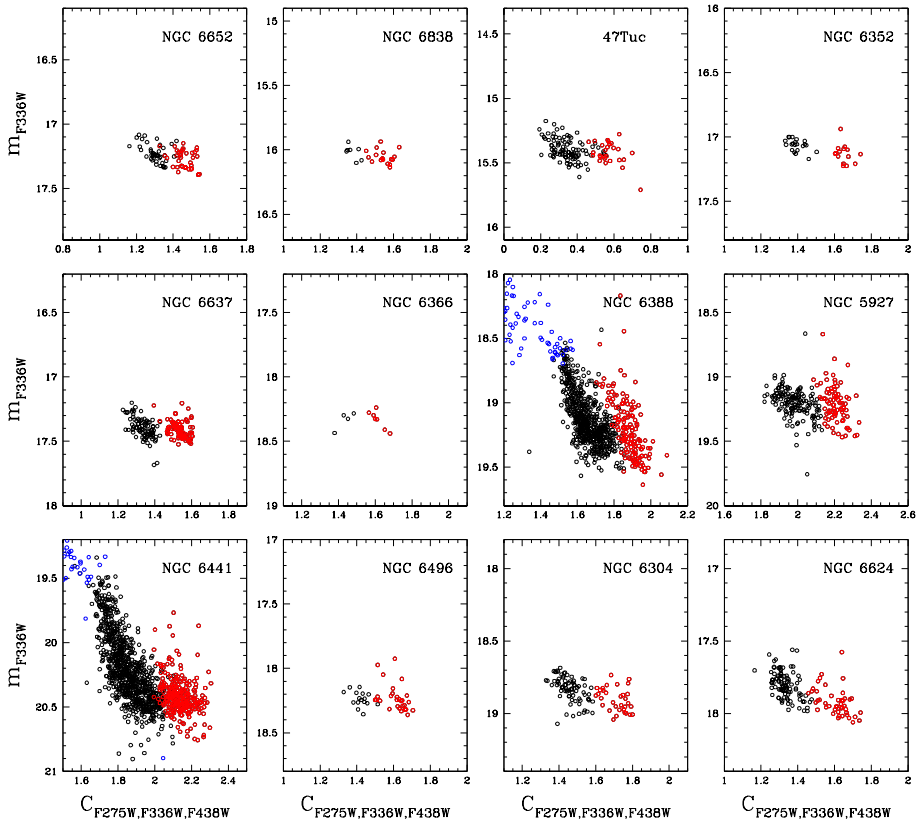

Figure 3.5: $m_{\rm F336W}$ vs. $C_{F275W,F336W,F438W}$ pseudo-CMDs for the studied Galactic GCs. 1G and 2G stars are coloured in red and black, respectively, while blue crosses mark bHB stars of NGC 6388 and NGC 6441.

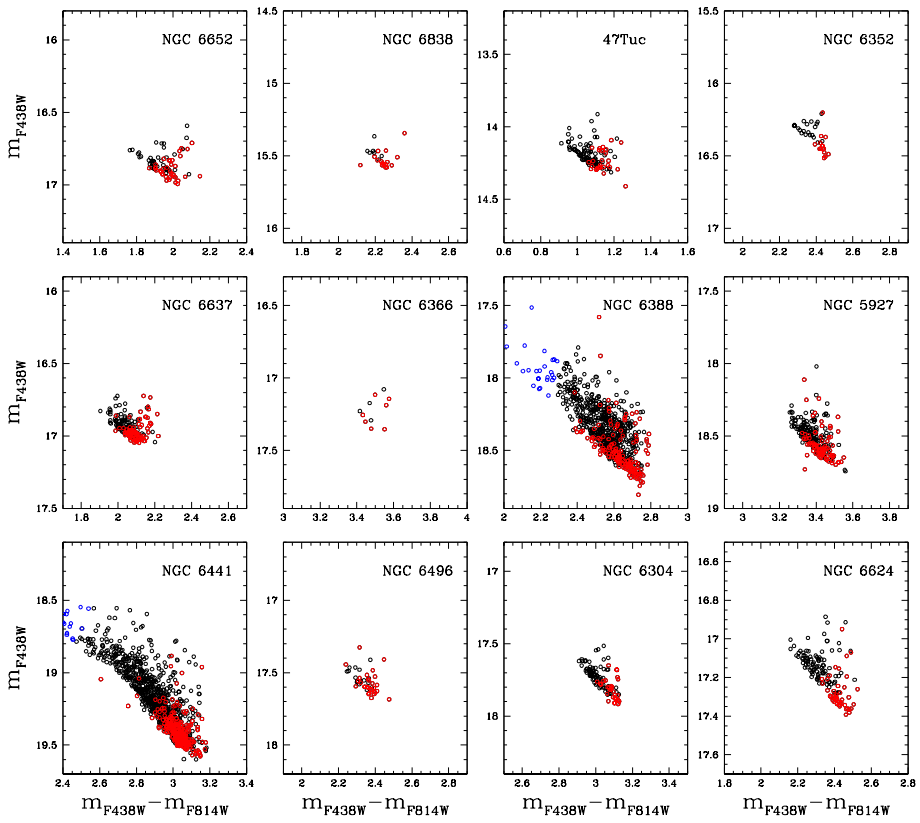

Figure 3.6: Optical $m_{\rm F438W}$ vs. $m_{\rm F438W} - m_{\rm F814W}$ CMDs of the studies clusters. Red, black and blue colors indicate 1G stars, 2G rHB stars, and 2G bHB stars, respectively.

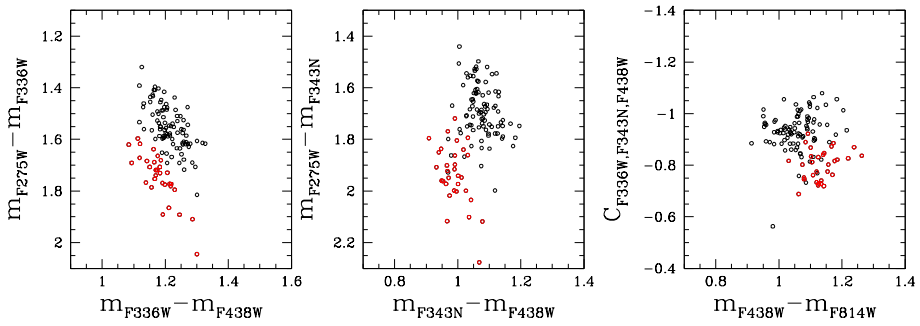

Figure 3.7: 1G and 2G stars of 47Tuc in three different two-colour diagrams. The 1G and 2G cluster stars selected in the $(m_{F275W} - m_{F336W})$ vs $(m_{F336W} - m_{F438W})$ (left panel), appear well separated also in the $(m_{F275W} - m_{F343N})$ vs $(m_{F343N} - m_{F438W})$ (central panel) and $C_{F336W,F343N,F438W}$ vs $m_{F438W} - m_{F814W}$ (right panel) two-colour diagrams.

F343N, which is a narrow filter that comprises the spectral region that includes various NH and molecular bands, is more sensitive than F336W to stellar populations with different nitrogen abundances. Hence, I exploited this filter to build the two-color $(m_{F275W} - m_{F343N})$ vs $(m_{F343N} - m_{F438W})$ diagram and the $C_{F336W,F343N,F438W} = (m_{F336W} - m_{F343N}) - (m_{F343N} - m_{F438W})$ vs $m_{F438W} - m_{F814W}$ pseudo two-color diagram for red HB stars.

Results are illustrated in Figure 3.7 for 47 Tuc, where we compare the classic $(m_{F275W} - m_{F336W})$ vs $(m_{F336W} - m_{F438W})$ two-color diagram with the diagrams introduced in this work. Clearly, the fact that 1G and 2G stars (red and black points in Figure 3.7) populate distinct regions in each diagram, demonstrates that the two-colour and pseudo two-color diagrams that involve photometry in F343N are powerful tools to detect multiple populations along the red HB.

3.3.2 Extragalactic Globular Clusters

Our cluster sample includes two extragalactic GCs, namely NGC 416 in the Small Magellanic Cloud and NGC 1978 in the Large Magellanic Cloud. For both clusters we exploited photometry in four bands, namely F275W, F336W, F343N and F438W, to build the three diagrams introduced in Section 3.3.1 for 47 Tuc. These diagrams are shown in Figure 3.8 and Figure 3.9, for NGC 416 and NGC 1978, respectively. For completeness, we compare in Figure 3.10 the m_{F336W} vs $C_{F275W,F336W,F438W}$ pseudo-CMDs of the rHB stars of these two clusters. All diagrams reveal that both NGC 416 and NGC 1978 host multiple populations along the rHB.

In contrast with what is observed in the majority of Galactic GCs, which are dominated by the 2G, the majority of rHB stars in both NGC 416 and NGC 1978 belong to the first generation. In particular, in NGC 1978 the fraction of 1G stars is close to 0.8.

Moreover, we notice that while 2G stars are significantly brighter and bluer than the 1G in the optical CMDs of Galactic clusters, stars of both populations are spread along the whole HB (Figure 3.11). This fact could indicate neg-

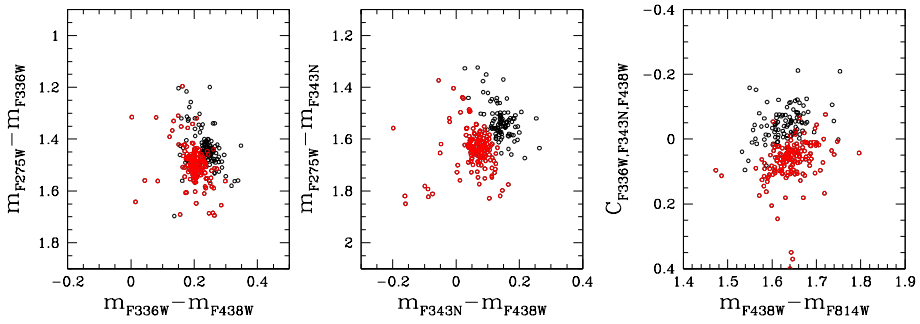

Figure 3.8: As in Figure 3.7 but for the SMC cluster NGC 416.

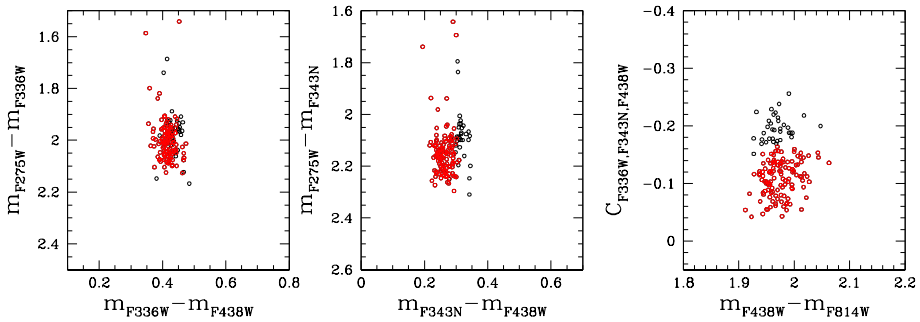

Figure 3.9: As in Figure 3.7 but for the LMC cluster NGC 1978.

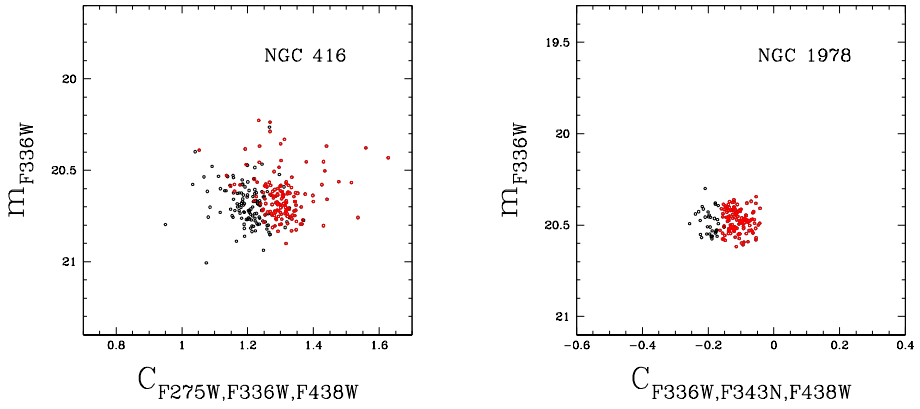

Figure 3.10: Comparison of the $m_{\rm F336W}$ vs. $C_{\rm F275W,F336W,F438W}$ pseudo CMDs of the extragalactic GCs NGC 416 and NGC 1978. The 1G stars are coloured in red and the 2G stars in black.

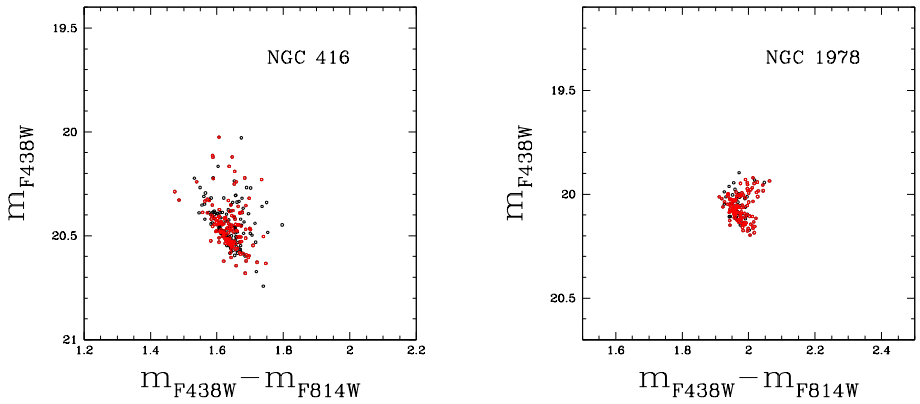

Figure 3.11: Comparison of the rHBs of the extragalactic clusters in optical CMDs. 1G stars are colored in red.

ligible helium differences between the two stellar populations of NGC 416 and NGC 1978.

3.4 NGC 6362

NGC 6362, which is the most metal-poor cluster of our sample ($[Fe/H] = -0.99$), deserves a separate analysis because of the specific morphology of its HB. The m_{F438W} vs $(m_{F438W} - m_{F814W})$ CMD has been plotted in the upper panel of Figure 3.12 and reveals that this cluster exhibit both the rHB and the bHB. Interestingly, in the $m_{F336W} - m_{F438W}$ vs $m_{F275W} - m_{F336W}$ two color diagram in the lower left panel, no split in rHB is visible.

To better investigate multiple populations along the HB of NGC 6652, I compared its two-color diagram with that of NGC 6652, a Galactic GC with similar metallicity ($[Fe/H] = -0.81$)

To do so, median value of rHB stars in NGC 6362 and of 1G stars in NGC 6352 have been calculated in both axis of the two-colour diagrams. Then, measuring the difference along the two axis, the median value of NGC 6352 has been shifted, superimposing it to the median value of NGC 6362.

The rHB stars of NGC 6362 are consistent with a single sequence and clearly overlap the 1G rHB stars of NGC 6652, thus suggesting that the rHB of NGC 6362 is only populated by 1G stars. Hence, NGC 6362 resembles the case of M 4, where the HB is well populated on both sides of the RR Lyrae instability strip. Based on high-resolution spectroscopy of HB stars, Marino et al. (2011) found that the rHB is populated by 1G stars, whereas the bHB is composed of 2G stars. Therefore, in order to estimate N_{1G}/N_{TOT} of NGC 6362, we assumed that the bHB is entirely composed of 2G stars (in blue in all three panels of Figure 3.12), in close analogy with what is observed in M 4.

3.5 NGC 6388 and NGC 6441

NGC 6388 and NGC 6441 have been traditionally considered as twin clusters. In fact, they share very similar masses, metallicities ($[Fe/H] \sim -0.50$), and they are both located in the Galactic bulge. The existence of bHB stars in these clusters was an unexpected feature given their relatively high metallicity (e.g. Rich et al. 1997) and was considered a signature of stellar populations with extreme helium abundances (e.g. D'Antona & Caloi 2008).

On the contrary, the comparison of the rHBs of NGC 6388 and NGC 6441 reveals some intriguing differences between the two clusters. We plot in Figure 3.13 the $C_{F275W,F336W,F438W}$ vs m_X diagram of HB stars in NGC 6388 (at left) and NGC 6441 (at right), where $X = F275W, F336W, F438W, F814W$. Their HBs have similar magnitude extension when I use optical filters. Moving progressively towards UV magnitudes (from the lower to the higher panels in Figure 3.13), the two HBs become more and more different. In NGC 6388, the distribution of 1G stars extends over a wider magnitude range with respect to those of NGC 6441. Moreover, the distribution of the 1G stars of NGC 6388 seems to indicate a split.

To emphasize the differences between the HBs of NGC 6388 and NGC 6441 in the two-colour diagram of Figure 3.14, the 1G sequence of NGC 6388 has been superimposed to that of NGC 6441. To do this, the median of $m_{F336W} - m_{F438W}$ and $m_{F275W} - m_{F336W}$ of 2G stars in both clusters have been calculated. Then, all the stars of NGC 6441 HB have been shifted by the difference between the two medians, so that 1G sequences of the two GCs are superimposed. The 1G stars of

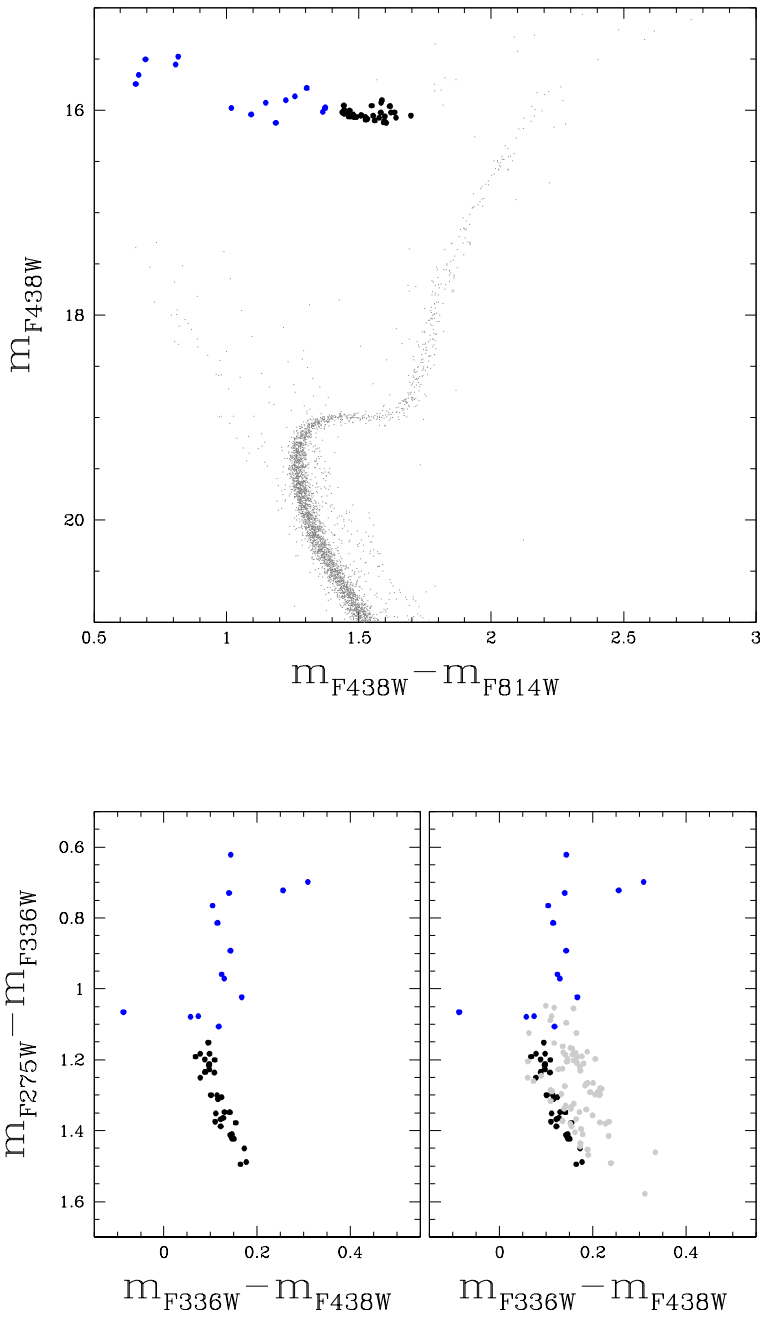

Figure 3.12: In the upper panel, the CMD of NGC 6362 is presented, with rHB stars in black and bHB stars in blue. The two-colour diagram of the cluster is shown in the lower left panel. Then, a comparison with the rHB of NGC 6352, for which stars have been coloured in grey, is made in the lower right panel. The distribution of gray stars is clearly wider than the black ones, indicating that the rHB of NGC 6362 is only made by 1G stars.

NGC 6388 with extreme values of $m_{F275W} - m_{F336W}$ have been coloured in aqua in Figure 3.14 (left panel). These stars, which are not present in NGC 6441, have then been plotted in the right panel, showing that the peculiar stars in two-colour diagram correspond to the stars with brighter UV magnitudes in the m_{F275W} vs $C_{F275W,F336W,F438W}$ diagram.

An appropriate interpretation of the difference morphology of the 1G sequences in the 'twin' clusters NGC 6388 and NGC 6441 would require the comparison of the observations with appropriate HB models (e.g. Tailo et al. 2017), and is beyond the purpose of my thesis.

However, I notice that as found in Milone et al. (2017), NGC 6388 is a Type II cluster, while NGC 6441 is a Type I cluster. From a photometric point of view, a Type II cluster presents split SGB and multi-modal ChM, which are associated with star-to-star variation in Fe, total C+N+O abundance and s-process elements. Similarly to most Type II clusters, the ChM of NGC 6388 exhibits an extended 1G sequence, whose nature is still debated. Internal variation in helium or metallicity as well as binary stars are considered possible responsible for the extension of the 1G in the ChM. In contrast, the 1G of NGC 6441 is consistent with a simple population. Results from this paper make it tempting to conclude that the same phenomenon is responsible for the difference between the morphology of 1G stars in NGC 6388 and NGC 6441 along the rHB and the different morphology of their ChMs.

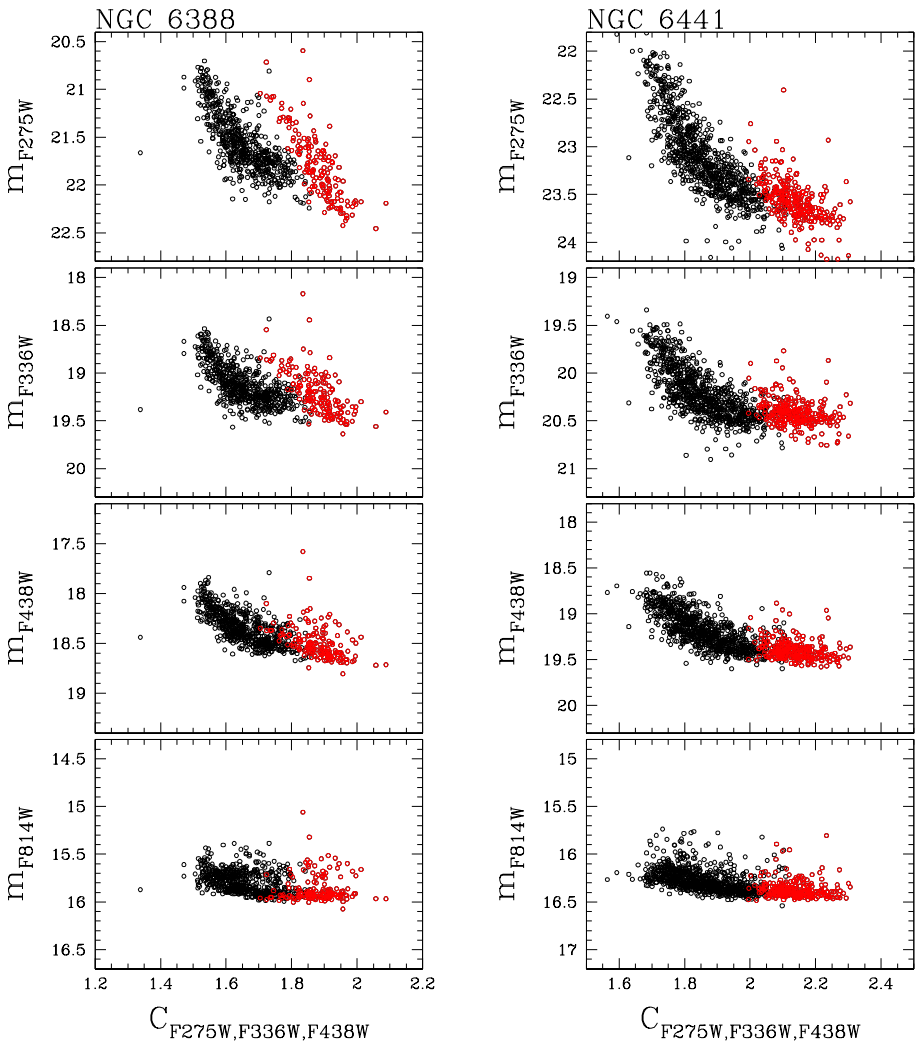

Figure 3.13: Comparison between the HBs of NGC 6388 (at left) and NGC 6441 (at right). The 1G stars have been plotted in red. Different magnitudes have been plotted against the $C_{F275W,F336W,F438W}$ index. In optical magnitudes the morphology of the HB of the two clusters is similar, while moving towards UV filters (higher panels) they show differences. While the 2G stars distribution does not vary a lot between the two clusters, the 1G stars in NGC 6388 are spread over a larger area in the diagram when considering UV magnitudes at the ordinate. The case in filter $F275W$ is the most evident.

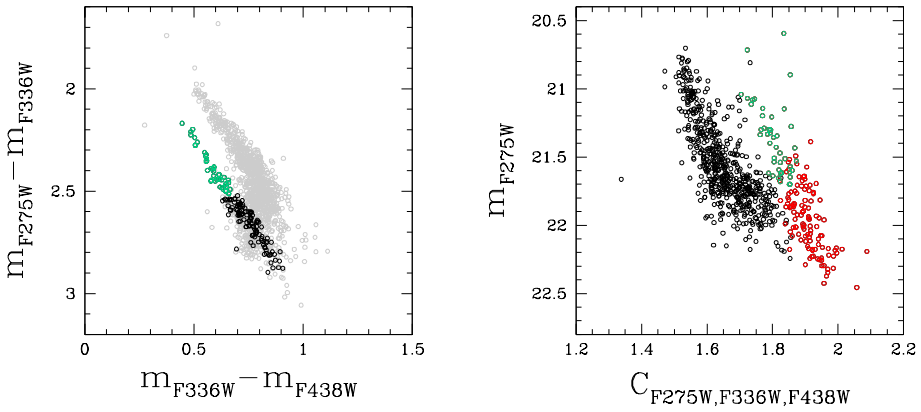

Figure 3.14: Left panel compares the rHB of NGC 6441 (gray points) with the rHB 1G stars of NGC 6388. The 1G stars of NGC 6388 with extreme values of $m_{F275W} - m_{F336W}$ have been colored aqua, while black dots represent the remaining 1G stars of NGC 6388. Right panel shows the m_{F275W} vs $C_{F275W,F336W,F438W}$ diagram of NGC 6388, where the 1G stars with extreme $m_{F275W} - m_{F336W}$ values have been coloured aqua, and the remaining 1G stars are coloured red.

Chapter 4

Discussion and conclusion

In this Chapter I discuss the results obtained in my analysis to constrain the role of the environment and the redshift on the multiple-population phenomenon. To do this, in the Section 4.1, I explore the correlations between the fraction of 1G stars and various parameters of the host GCs, including present-day and initial mass, age and perigalactic distance. In Section 4.2 I extend the analysis to literature determination of the fraction of 1G stars obtained from different techniques. Finally, In Section 4.3 I summarize the main results of this thesis.

4.1 Correlations with Cluster Parameters

To shed light on the role of the environment and the formation redshift on the MPs phenomenon, the fractions of 1G stars derived in this work have been compared with those cluster parameters, that are more relevant in the context of multiple-population studies (see discussion by Milone et al. 2017). Firstly, N_{1G}/N_{TOT} is compared with the values of present-day (M) and initial mass (M_i). These two quantities have been taken from the results obtained in Baumgardt & Hilker (2018) and Goudfrooij et al. (2014). In Figure 4.1 I plotted the values of N_{1G}/N_{TOT} derived from the rHB stars against M and M_i. Black points indicate the Galactic clusters in our sample, while red points the extragalactic GCs. It is clear, from the diagrams, that the fraction of 1G stars anticorrelates with both the present-day and the initial mass. This is confirmed also considering, for Galactic clusters, the Spearman's rank correlation coefficient between M and N_{1G}/N_{TOT}, that is $R_s = -0.80$, and between M_i and N_{1G}/N_{TOT}, that is $R_s = -0.81$.

These results suggest also that, at the same value of M and M_i, the extragalactic GCs have a larger N_{1G}/N_{TOT} than the Galactic ones. In particular, NGC 1978 is dominated by 1G stars, which comprise about 80% of the total number of cluster stars.

It is also interesting to notice the large difference between fractions of the two extragalactic clusters, of almost 0.20. NGC 1978 has a significant higher fraction of 1G stars than NGC 416 even though the first have an higher mass with respect to the second. Interestingly, the ∼2 Gyr-old cluster NGC 1978 is significantly younger than NGC 416, which has age of ∼ 6 Gyr.

Figure 4.2 shows N_{1G}/N_{TOT} against the cluster age diagram, using ages

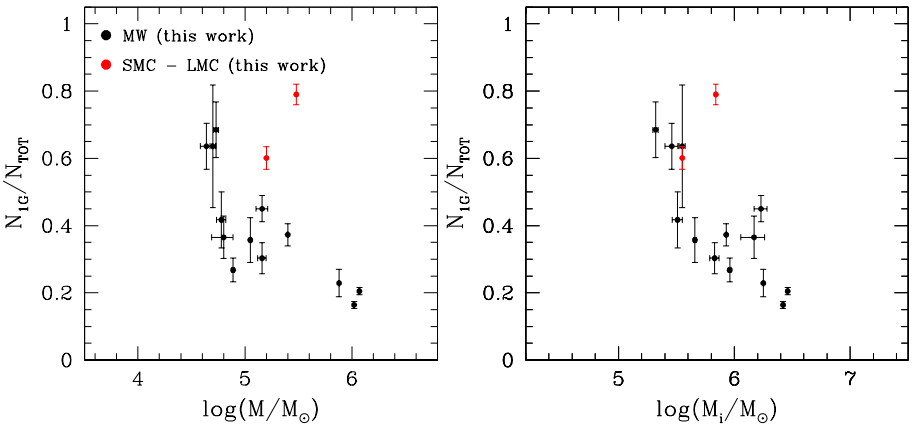

Figure 4.1: The fractions of 1G stars calculated in this work from the rHB stars are plotted against the present-day mass (left) and the initial mass (right). The Galactic GCs are shown in black, while red dots indicate the extragalactic clusters.

from Dotter et al. (2010) for the Galactic clusters and from Milone et al. (2009) and Lagioia et al. (2019) for the extragalactic clusters. The Spearman's rank correlation coefficient is $R_s = -0.72$.

In Figure 4.3, I show N_{1G}/N_{TOT} vs the perigalactic radius (R_{PER}) for Galactic GCs alone. Using R_{PER} values from Baumgardt et al. (2019), no significant correlations has been revealed. The Spearman's rank correlation coefficient is $R_s = 0.36$.

4.2 Comparison with the literature

The fractions of 1G stars found in Galactic GCs are summarized in Table 4.1, in which they have also been compared with the values obtained by Milone et al. (2015) and Milone et al. (2020b), by using respectively RGB and MS stars.

The same results found in extragalactic GCs are summarized in Table 4.2, in which the fractions of 1G stars have been compared to the one measured in Milone et al. (2020a).

In Figure 4.4 I plotted the values here calculated against the ones from literature. Only two of the analysed clusters are not consistent within errorbars. The first is NGC 6388, where the fraction measured is lower with respect to the literature. The second is NGC 416, where the fraction measured is higher. The latter can be explained considering that, performing its data reduction, new observations have been added with respect to previous works in literature. So it is possible that a different dataset may give different results. The case of NGC 6388 is more complicated. The difference between the two values could be a consequence of the fact that the cluster is Type II, and in some way this brings to different ratios when considering HB and RGB stars.

It is now useful to combine the results here obtained with previous works in literature, in order to consider a larger sample of clusters. In Figure 4.5, the N_{1G}/N_{TOT} vs M and M_i diagrams have been plotted using values found in this

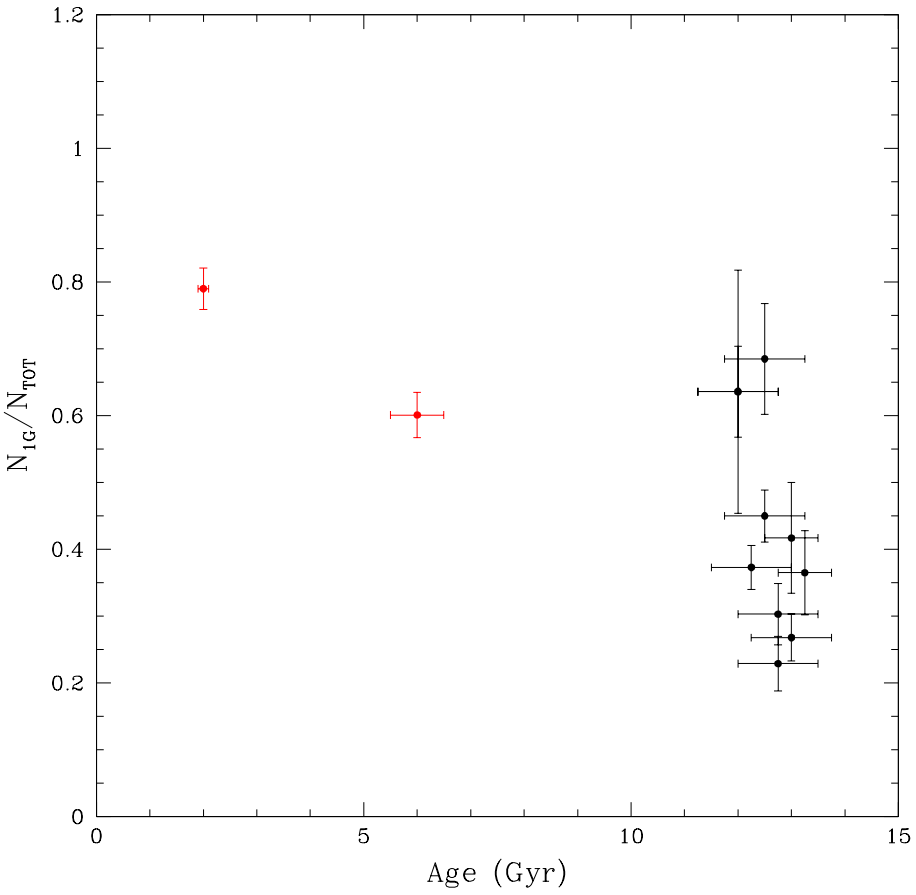

Figure 4.2: Fraction of 1G stars as a function of cluster age. Symbols are the same as in Figure 4.1.

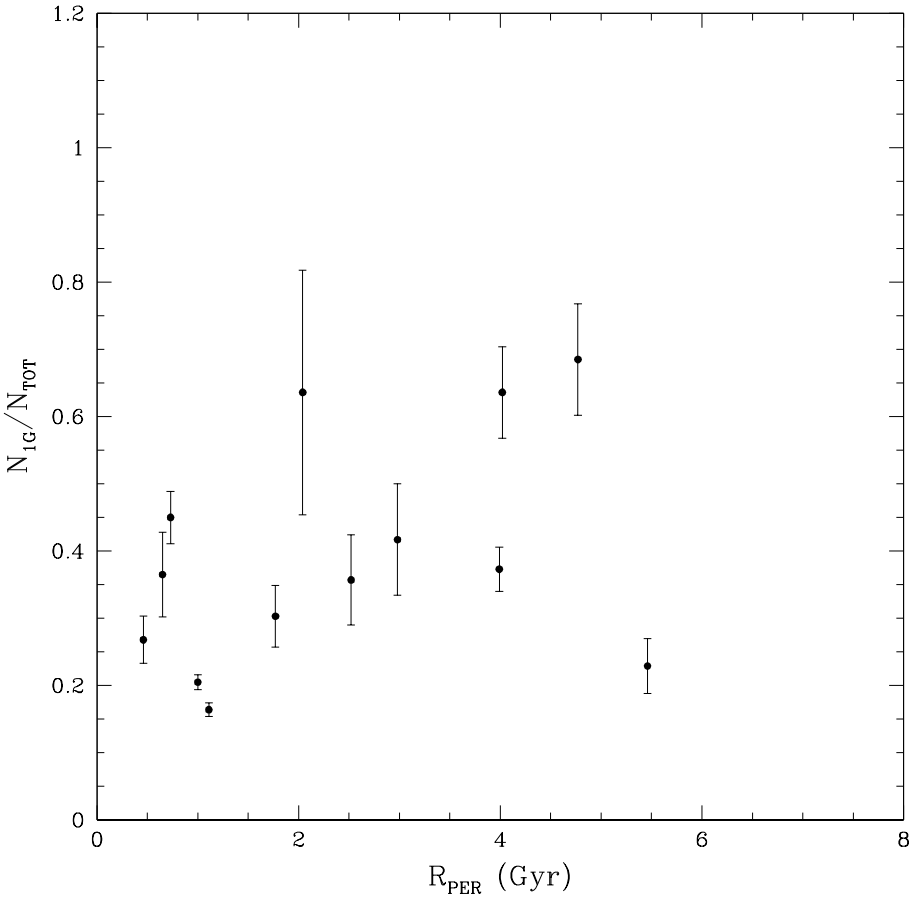

Figure 4.3: Fraction of 1G stars against the perigalactic radius of the Galactic clusters. Symbols are the same as in Figure 4.1.

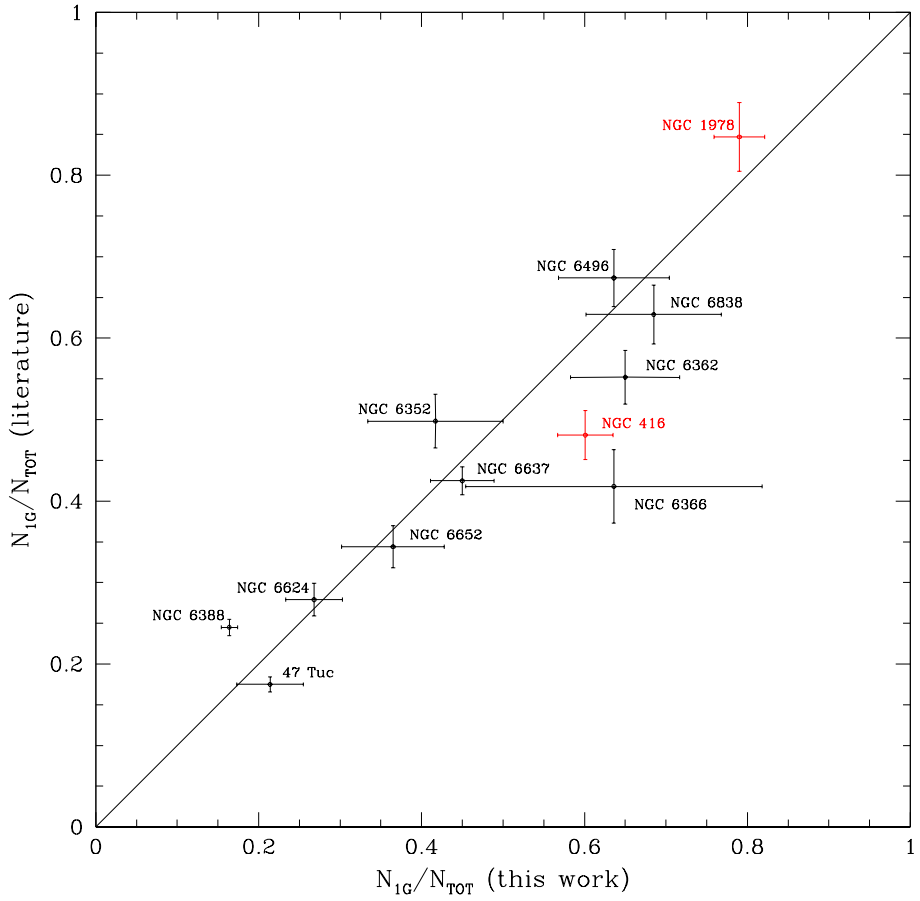

Figure 4.4: Comparison between the fraction of 1G stars measured in this work and the values from the literature. Galactic ones are represented with black dots, while the extragalactic GCs are shown in red.

work, Milone et al. (2017), Milone et al. (2020a) and Milone et al. (2020b). For the clusters in common with other works, I decided to plot the weighted average of N_{1G}/N_{TOT} values when they are consistent within errorbars. The two values of NGC 6388 have both been plotted as the two gray triangles connected with a gray line. The value of NGC 416 considered is the one in this work, since it is based on a larger dataset with respect to the previous works in literature. I highlight again that I also estimated for the first time the fraction of 1G stars in the Galactic GCs NGC 5927, NGC 6304 and NGC 6441.

The observed trend confirms the previous finding that the fraction of 1G stars ancticorrelates with the present-day and the initial cluster mass.

Finally, the same approach has been used to verify the correlation between age of clusters and fraction of 1G stars found. The ages used have been taken from Dotter et al. (2010). As before, I do not find any clear trend. In fact, the Spearman's rank correlation index is $R_s = -0.18$, thus indicating no monotonic correlation. This diagram is shown in Figure 4.6.

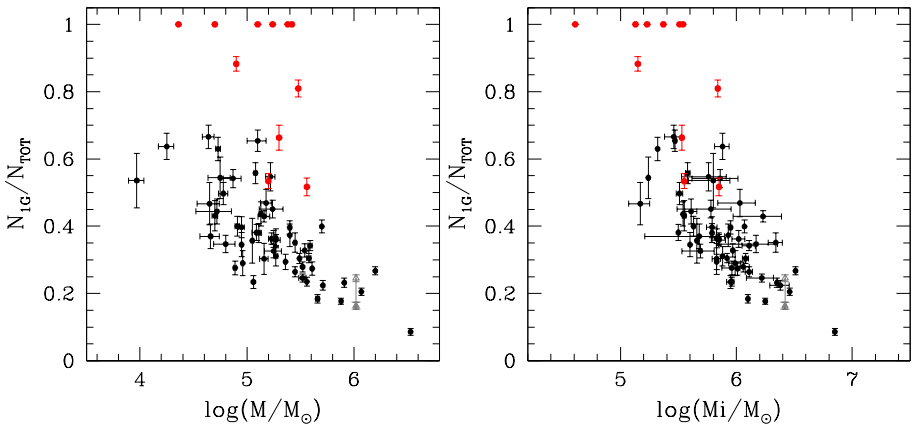

Figure 4.5: Fraction of 1G stars versus the present-day and the initial mass, obtained combining values from Milone et al. (2017), Milone et al. (2020a) and Milone et al. (2020b) from RGB and MS stars with the those measured in this work from HB stars. In case of GCs with multiple estimate of N_{1G}/N_{TOT}, a weighted average is considered if the values are consistent within the errorbars. The filled and the open triangles, connected with a gray line, indicate respectively the measure here obtained and the value obtained in Milone et al. (2017), which are not consistent each others.

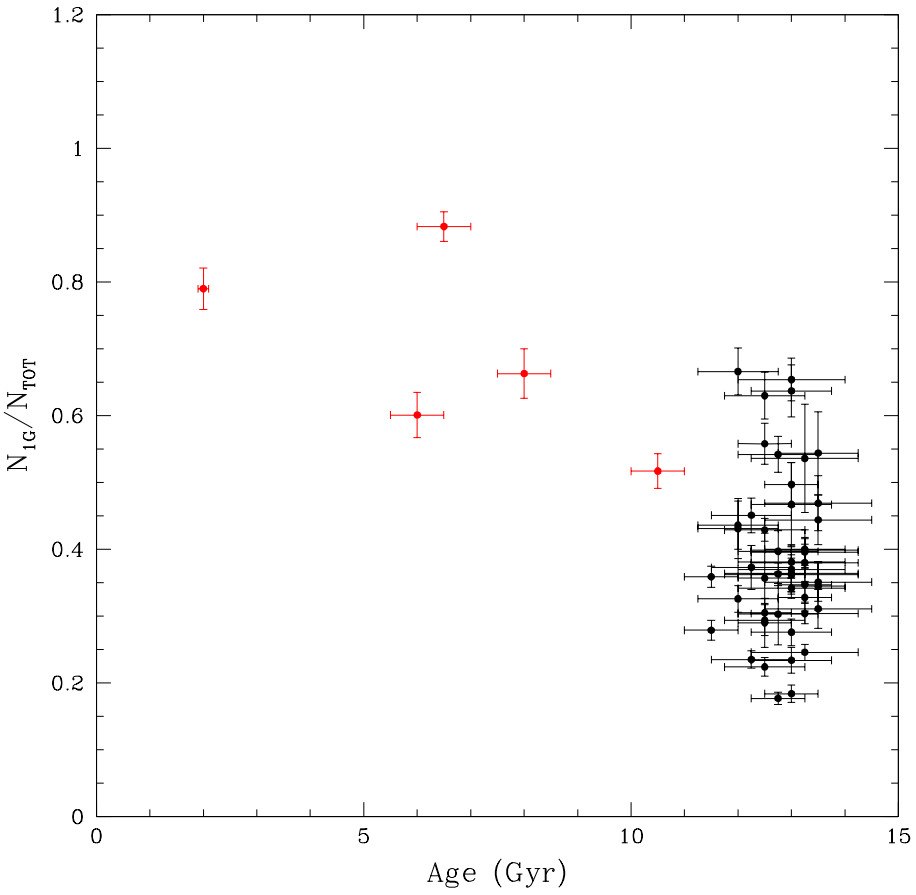

Figure 4.6: Fraction of 1G stars plotted against to the cluster age. The Galactic and MC GCs are coloured in black and red, respectively.

4.3 Summary and Conclusions

In this work, I introduced a new method for the estimate of the fraction of 1G and 2G stars in GCs, based on the distribution of red HB stars in UV-optical two-colour diagrams. This allowed me to identify and characterize, for the first time, the MPs along the red HB in a large sample of $\sim$ 13-Gyr old Galactic GCs and in the extragalactic GCs NGC 416 and NGC 1978, which have ages of $\sim$2 and $\sim$6 Gyr, respectively. The main goal of the thesis is investigating the role of redshift and environment on the mupliple-population phenomenon.

To do this, I exploited multi-band photometry obtained from images collected with the ACS/WFC and WFC3/UVIS cameras on board *HST*. In particular, I derived high-precision astrometry and multi-band photometry of stars in the field of view of the SMC cluster NGC 416 by using the methods and the computer programs developed by Jay Anderson at the Space Telescope Science Institute. The main results can be summarized as follows:

- I identified distinct sequences of 1G and 2G stars along the rHB of fifteen Milky-Way GCs, of the NGC 416 in the SMC and NGC 1978 in the LMC. This results confirm that MPs are common features of both Galactic and extragalactic GCs.

- Multiple populations along the rHB exhibit a huge variety, with the extension of the 1G and 2G sequences, the number of sub-populations and the relative number of stars in each population, changing from one cluster to another. This fact corroborates the evidence that the MP phenomenon exhibit a huge complexity.

- I measured the fraction of 1G stars, by using for the first time the rHB. The fraction of 1G stars in Milky Way clusters ranges from $\sim$15% in the massive GC NGC 6388 to $\sim$68% in the low-mass cluster NGC 6838. Noticeably, by using HB stars, it was possible for the first time to measure the population ratios in NGC 5927, NGC 6304 and NGC 6441.

- My results on rHB stars show that the fraction of 1G stars in Galactic GCs correlate with the present day and the initial mass of the host cluster, with massive GCs having larger fraction of 2G stars. This result is confirmed also when we enlarge the number of clusters by including literature determination of the fraction of 1G star inferred from the RGB. This fact demonstrates that the incidence and complexity of the multiple population phenomenon depend on GC mass.

- I discovered that NGC 6388 exhibit an extended 1G sequence in the $m_{F336W} - m_{F438W}$ vs $m_{F275W} - m_{F336W}$ two color diagram, in contrast with what is observed in NGC 6441, which is considered its 'twin' cluster. I speculate that internal $C + N + O$ variation would be responsible for the extended 1G of NGC 6441.

- The fraction of 1G stars in the extragalactic clusters NGC 416 and NGC 1978 are ~ 0.6 and ~ 0.8 and are larger than those of Galactic GCs with similar masses, which are typically dominated by the second generation.

- When I combine results from the old Galactic GCs and the young and intermediate LMC and SMC cluster, I find a mild correlation between

the fraction of 1G stars and the cluster age, hence the redshift of the cluster-formation epoch. However, enlarging the sample using results in literature, I find many old GCs with similar fraction of 1G stars as young and intermediate-age clusters of the Magellanic Clouds.

The results are consistent with a scenario in which the GCs are dominated by the 1G at formation and most 1G stars are stripped away from the cluster due to interaction with the host galaxy. Indeed, in this scenario, we expect that the studies LMC and SMC clusters, which are younger than Milky-Way GCs, are still dominated by the 1G. Moreover, due to their relatively small masses, the Magellanic Clouds would be less efficient than the Milky Way in striping 1G stars from their GCs.

Table 4.1: Fractions of 1G stars calculated in this work, found in literature and a weighted average of both results for the galactic GCs.

CLUSTER	N_{1G}/N_{TOT} (this work)	N_{1G}/N_{TOT} (literature)	N_{1G}/N_{TOT} (averaged)
NGC 0104	0.229 ± 0.041	0.175 ± 0.009	0.177 ± 0.009
NGC 0288	–	0.558 ± 0.030	0.558 ± 0.031
NGC 0362	–	0.279 ± 0.015	0.279 ± 0.015
NGC 1261	–	0.359 ± 0.016	0.359 ± 0.016
NGC 1851	–	0.264 ± 0.015	0.264 ± 0.015
NGC 2298	–	0.370 ± 0.037	0.370 ± 0.037
NGC 2808	–	0.232 ± 0.014	0.232 ± 0.014
NGC 3201	–	0.436 ± 0.036	0.436 ± 0.036
NGC 4590	–	0.381 ± 0.024	0.381 ± 0.024
NGC 4833	–	0.362 ± 0.025	0.362 ± 0.025
NGC 5024	–	0.328 ± 0.020	0.328 ± 0.020
NGC 5053	–	0.544 ± 0.062	0.544 ± 0.062
NGC 5139	–	0.086 ± 0.010	0.086 ± 0.010
NGC 5272	–	0.305 ± 0.014	0.305 ± 0.014
NGC 5286	–	0.342 ± 0.015	0.342 ± 0.015
NGC 5466	–	0.467 ± 0.063	0.467 ± 0.063
NGC 5897	–	0.547 ± 0.042	0.547 ± 0.042
NGC 5904	–	0.235 ± 0.013	0.235 ± 0.013
NGC 5927	0.373 ± 0.033	–	0.373 ± 0.033
NGC 5986	–	0.246 ± 0.012	0.246 ± 0.012
NGC 6093	–	0.351 ± 0.029	0.351 ± 0.029
NGC 6101	–	0.654 ± 0.032	0.654 ± 0.032
NGC 6121	–	0.290 ± 0.035	0.290 ± 0.037
NGC 6144	–	0.444 ± 0.037	0.444 ± 0.037
NGC 6171	–	0.397 ± 0.031	0.397 ± 0.031
NGC 6205	–	0.184 ± 0.013	0.184 ± 0.013
NGC 6218	–	0.400 ± 0.029	0.400 ± 0.029
NGC 6254	–	0.364 ± 0.028	0.364 ± 0.028
NGC 6304	0.303 ± 0.046	–	0.303 ± 0.046
NGC 6341	–	0.304 ± 0.015	0.304 ± 0.015
NGC 6352	0.417 ± 0.083	0.498 ± 0.033	0.497 ± 0.033
NGC 6362	$\pm$	0.552 ± 0.033	0.357 ± 0.067
NGC 6366	0.455 ± 0.182	0.418 ± 0.045	0.420 ± 0.045

CLUSTER	N_{1G}/N_{TOT} (this work)	N_{1G}/N_{TOT} (literature)	N_{1G}/N_{TOT} (total)
NGC 6388	0.149 ± 0.010	0.245 ± 0.010	–
NGC 6397	–	0.345 ± 0.036	0.345 ± 0.036
NGC 6441	0.205 ± 0.011	–	0.205 ± 0.011
NGC 6496	0.636 ± 0.068	0.674 ± 0.035	0.666 ± 0.035
NGC 6535	–	0.536 ± 0.081	0.536 ± 0.081
NGC 6541	–	0.396 ± 0.020	0.396 ± 0.020
NGC 6584	–	0.451 ± 0.026	0.451 ± 0.026
NGC 6624	0.268 ± 0.035	0.279 ± 0.020	0.276 ± 0.020
NGC 6637	0.450 ± 0.039	0.425 ± 0.017	0.429 ± 0.017
NGC 6652	0.365 ± 0.063	0.344 ± 0.026	0.347 ± 0.026
NGC 6656	–	0.274 ± 0.020	0.274 ± 0.020
NGC 6681	–	0.234 ± 0.019	0.234 ± 0.019
NGC 6715	–	0.267 ± 0.012	0.267 ± 0.012
NGC 6717	–	0.637 ± 0.039	0.637 ± 0.039
NGC 6723	–	0.363 ± 0.017	0.363 ± 0.017
NGC 6752	–	0.294 ± 0.023	0.294 ± 0.023
NGC 6779	–	0.469 ± 0.041	0.469 ± 0.041
NGC 6809	–	0.311 ± 0.029	0.311 ± 0.029
NGC 6838	0.685 ± 0.083	0.629 ± 0.036	0.630 ± 0.035
NGC 6934	–	0.326 ± 0.020	0.326 ± 0.020
NGC 6981	–	0.542 ± 0.027	0.542 ± 0.027
NGC 7078	–	0.399 ± 0.019	0.399 ± 0.019
NGC 7089	–	0.224 ± 0.014	0.224 ± 0.014
NGC 7099	–	0.380 ± 0.028	0.380 ± 0.028

Table 4.2: Fractions of 1G stars calculated in this work, found in literature and a weighted average of both results for the extragalactic GCs.

CLUSTER	N_{1G}/N_{TOT} (this work)	N_{1G}/N_{TOT} (literature)	N_{1G}/N_{TOT} (averaged)
Lindsay 1	–	0.663 ± 0.037	0.663 ± 0.037
Lindsay 38	–	1.000	1.000
Lindsay 113	–	1.000	1.000
NGC 0121	–	0.517 ± 0.026	0.517 ± 0.026
NGC 0339	–	0.883 ± 0.022	0.883 ± 0.022
NGC 0416	0.601 ± 0.034	0.481 ± 0.030	–
NGC 0419	–	1.000	1.000
NGC 1783	–	1.000	1.000
NGC 1806	–	1.000	1.000
NGC 1846	–	1.000	1.000
NGC 1978	0.790 ± 0.031	0.847 ± 0.042	0.810 ± 0.025

Bibliography

Anderson, J. & King, I. R. 2000, PASP, 112, 1360

Anderson, J. & King, I. R. 2006, PSFs, Photometry, and Astronomy for the ACS/WFC, Instrument Science Report ACS 2006-01

Anderson, J., King, I. R., Richer, H. B., et al. 2008, AJ, 135, 2114

Bastian, N., Kamann, S., Cabrera-Ziri, I., et al. 2018, MNRAS, 480, 3739

Bastian, N., Lamers, H. J. G. L. M., de Mink, S. E., et al. 2013, MNRAS, 436, 2398

Baumgardt, H. & Hilker, M. 2018, MNRAS, 478, 1520

Baumgardt, H., Hilker, M., Sollima, A., & Bellini, A. 2019, MNRAS, 482, 5138

Behr, B. B. 2003, ApJS, 149, 67

Bellini, A., Libralato, M., Bedin, L. R., et al. 2018, ApJ, 853, 86

Bellini, A., Piotto, G., Bedin, L. R., et al. 2009, A& A, 507, 1393

Cabrera-Ziri, I., Martocchia, S., Hollyhead, K., & Bastian, N. 2018, Memorie della Societa Astronomica Italiana, 89, 24

Carretta, E., Bragaglia, A., Gratton, R. G., et al. 2009, A&A, 505, 117

Cohen, J. G. & Melendez, J. 2005, AJ, 129, 1607

Cordero, M. J., Pilachowski, C. A., Johnson, C. I., et al. 2014, ApJ, 780, 94

Cordoni, G., Milone, A. P., Marino, A. F., et al. 2018, ApJ, 869, 139

Cordoni, G., Milone, A. P., Mastrobuono-Battisti, A., et al. 2019, arXiv e-prints, arXiv:1908.11692

Dalessandro, E., Mucciarelli, A., Bellazzini, M., et al. 2018, ApJ, 864, 33

D'Antona, F. & Caloi, V. 2008, MNRAS, 390, 693

D'Antona, F., Caloi, V., Montalbán, J., Ventura, P., & Gratton, R. 2002, A&A, 395, 69

D'Antona, F., Di Criscienzo, M., Decressin, T., et al. 2015, MNRAS, 453, 2637

de Mink, S. E., Pols, O. R., Langer, N., & Izzard, R. G. 2009, A&A, 507, L1

Denissenkov, P. A. & Hartwick, F. D. A. 2014, MNRAS, 437, L21

Denissenkov, P. A., VandenBerg, D. A., Hartwick, F. D. A., et al. 2015, MNRAS, 448, 3314

D'Ercole, A., D'Antona, F., Ventura, P., Vesperini, E., & McMillan, S. L. W. 2010, MNRAS, 407, 854

Dotter, A., Sarajedini, A., Anderson, J., et al. 2010, ApJ, 708, 698

Gaia Collaboration, Brown, A. G. A., Vallenari, A., et al. 2016a, A&A, 595, A2

Gaia Collaboration, Prusti, T., de Bruijne, J. H. J., et al. 2016b, A&A, 595, A1

Gieles, M., Charbonnel, C., Krause, M. G. H., et al. 2018, MNRAS, 478, 2461

Goudfrooij, P., Girardi, L., & Correnti, M. 2017, ApJ, 846, 22

Goudfrooij, P., Girardi, L., Kozhurina-Platais, V., et al. 2014, ApJ, 797, 35

Hollyhead, K., Kacharov, N., Lardo, C., et al. 2017, MNRAS, 465, L39

Krause, M., Charbonnel, C., Decressin, T., Meynet, G., & Prantzos, N. 2013, A&A, 552, A121

Lagioia, E. P., Milone, A. P., Marino, A. F., et al. 2018, MNRAS, 475, 4088

Lagioia, E. P., Milone, A. P., Marino, A. F., Cordoni, G., & Tailo, M. 2019, AJ, 158, 202

Lagioia, E. P., Milone, A. P., Marino, A. F., & Dotter, A. 2019b, ApJ, 871, 140

Lee, J.-W. 2018, ApJS, 238, 24

Marino, A. F., Milone, A. P., Przybilla, N., et al. 2014, MNRAS, 437, 1609

Marino, A. F., Milone, A. P., Renzini, A., et al. 2019, MNRAS, 487, 3815

Marino, A. F., Przybilla, N., Milone, A. P., et al. 2018, AJ, 156, 116

Marino, A. F., Sneden, C., Kraft, R. P., et al. 2011, A&A, 532, A8

Marino, A. F., Villanova, S., Piotto, G., et al. 2008, A&A, 490, 625

Martocchia, S., Bastian, N., Usher, C., et al. 2017, MNRAS, 468, 3150

Martocchia, S., Niederhofer, F., Dalessandro, E., et al. 2018, MNRAS, 477, 4696

Milone, A. P. 2019, arXiv e-prints, arXiv:1908.11703

Milone, A. P., Bedin, L. R., Piotto, G., & Anderson, J. 2009, A&A, 497, 755

Milone, A. P., Marino, A. F., Bedin, L. R., et al. 2019, MNRAS, 484, 4046

Milone, A. P., Marino, A. F., Cassisi, S., et al. 2012a, ApJL, 754, L34

Milone, A. P., Marino, A. F., Da Costa, G. S., et al. 2020a, MNRAS, 491, 515

Milone, A. P., Marino, A. F., Piotto, G., et al. 2013, ApJ, 767, 120

Milone, A. P., Marino, A. F., Piotto, G., et al. 2015, ApJ, 808, 51

Milone, A. P., Piotto, G., Bedin, L. R., et al. 2012b, A&A, 540, A16

Milone, A. P., Piotto, G., Bedin, L. R., et al. 2012c, A&A, 540, A16

Milone, A. P., Piotto, G., Bedin, L. R., et al. 2012d, ApJ, 744, 58

Milone, A. P., Piotto, G., Renzini, A., et al. 2017, MNRAS, 464, 3636

Milone, A. P., Vesperini, E., Marino, A. F., et al. 2020b, MNRAS, 492, 5457

Mucciarelli, A., Dalessandro, E., Ferraro, F. R., Origlia, L., & Lanzoni, B. 2014, ApJL, 793, L6

Nardiello, D., Libralato, M., Piotto, G., et al. 2018, MNRAS, 481, 3382

Nardiello, D., Milone, A. P., Piotto, G., et al. 2015, A & A, 573, A70

Niederhofer, F., Bastian, N., Kozhurina-Platais, V., et al. 2017, MNRAS, 464, 94

Piotto, G., Bedin, L. R., Anderson, J., et al. 2007, ApJL, 661, L53

Piotto, G., Milone, A. P., Bedin, L. R., et al. 2015, AJ, 149, 91

Renzini, A. 2013, Mem. Soc. Astron. Ital., 84, 162

Renzini, A., D'Antona, F., Cassisi, S., et al. 2015, MNRAS, 454, 4197

Rich, R. M., Sosin, C., Djorgovski, S. G., et al. 1997, ApJL, 484, L25

Richer, H. B., Heyl, J., Anderson, J., et al. 2013, ApJL, 771, L15

Sollima, A., Ferraro, F. R., Bellazzini, M., et al. 2007, ApJ, 654, 915

Tailo, M., D'Antona, F., Milone, A. P., et al. 2017, MNRAS, 465, 1046

Ventura, P., Di Criscienzo, M., Carini, R., & D'Antona, F. 2013, MNRAS, 431, 3642

Vesperini, E., McMillan, S. L. W., D'Antona, F., & D'Ercole, A. 2010, ApJL, 718, L112

Yong, D., Grundahl, F., Johnson, J. A., & Asplund, M. 2008, ApJ, 684, 1159

Zennaro, M., Milone, A. P., Marino, A. F., et al. 2019, MNRAS, 487, 3239